CENSORS: A Combined EIS-NVSS Survey Of Radio Sources. I. Sample definition, radio data and optical identifications

P. N. Best,[1][*] J. N. Arts[2], H. J. A. Röttgering[2], R. Rengelink[2], M. H. Brookes[1], J. Wall[3]

[1] *Institute for Astronomy, Royal Observatory Edinburgh, Blackford Hill, Edinburgh EH9 3HJ, UK*
[2] *Sterrewacht Leiden, Postbus 9513, 2300 RA Leiden, the Netherlands*
[3] *Department of Astrophysics, University of Oxford, Keble Road, Oxford, OX1 3RH, United Kingdom*

2 February 2008

ABSTRACT

A new sample of radio sources, with the designated name CENSORS (*A Combined EIS-NVSS Survey Of Radio Sources*), has been defined by combining the NRAO VLA Sky Survey (NVSS) at $1.4\,\mathrm{GHz}$ with the ESO Imaging Survey (EIS) Patch D, a 3 by 2 degree region of sky centred at 09 51 36.0, -21 00 00 (J2000). New radio observations of 199 NVSS radio sources with NVSS flux densities $S_{1.4\,GHz} > 7.8\,\mathrm{mJy}$ are presented, and compared with the EIS I–band imaging observations which reach a depth of $I \sim 23$; optical identifications are obtained for over two–thirds of the ~ 150 confirmed radio sources within the EIS field. The radio sources have a median linear size of 6 arcseconds, consistent with the trend for lower flux density radio sources to be less extended. Other radio source properties, such as the lobe flux density ratios, are consistent with those of brighter radio source samples. From the optical information, 30–40% of the sources are expected to lie at redshifts $z \gtrsim 1.5$.

One of the key goals of this survey is to accurately determine the high redshift evolution of the radio luminosity function. These radio sources are at the ideal flux density level to achieve this goal; at redshifts $z \sim 2$ they have luminosities which are around the break of the luminosity function and so provide a much more accurate census of the radio source population at those redshifts than the existing studies of extreme, high radio power sources. Other survey goals include investigating the dual–population unification schemes for radio sources, studying the radio luminosity dependence of the evolution of radio source environments, and understanding the radio power dependence of the K$-z$ relation for radio galaxies.

Key words: Surveys — galaxies: active — radio continuum: galaxies — galaxies: luminosity function

1 INTRODUCTION

The study of complete samples of radio sources can provide important information on the cosmic evolution of the number density, nature and physical properties of radio sources. For this reason, since the birth of radio astronomy considerable effort has been put into obtaining complete optical identifications and redshifts for flux–limited samples of sources selected at a variety of different observing frequencies and flux density levels (e.g. Laing, Riley & Longair 1983 Allington-Smith 1984, Spinrad et al. 1985, Eales 1985a, Wall & Peacock 1985, Dunlop et al. 1989, Lacy et al. 1993, McCarthy et al. 1996, Best, Röttgering & Lehnert 1999,2000, Waddington et al. 2001, Rawlings, Eales & Lacy 2001, Willott et al. 2002, and references therein).

An important study that can be carried out with such samples is to determine the cosmic evolution of the luminosity function of radio sources. In 1990, Dunlop & Peacock (1990) carried out a de-

tailed investigation of this, and presented the first evidence for a decline in the comoving number density of powerful radio sources beyond $z \sim 2.5$. Since this time, however, whilst numerous advances have provided a good consensus in the determination of the low redshift radio luminosity function (e.g. Mobasher et al. 1999, Gavazzi & Boselli 1999, Machalski & Godlowski 2000, Sadler et al. 2002), the high redshift evolution and the reality of the 'redshift cut-off' in the radio source population have remained areas of much controversy. Willott et al. (1998; 2001) found no evidence for a cut-off beyond $z \sim 2$ using the 7C radio survey (Pooley et al. 1998), whilst Bremer et al. (1999) claimed tentative indications of a redshift cut-off in a smaller sample of ultra-steep spectrum sources selected from the Westerbork Northern Sky Survey (WENSS; Rengelink et al. 1998) at similar luminosities. In more recent studies, Waddington et al. (2001) showed that a sample selected at the 1 mJy level does show evidence for a deficit of moderate luminosity radio sources at $z > 2$, but this sample had insufficient sky coverage to investigate the most luminous sources, while the sample of Jarvis et al. (2001) at the 100 mJy level proved too shallow to detect suf-

[*] Email: pnb@roe.ac.uk

ficient sources at high enough redshift to clarify the high-redshift evolution. It is clear that a radio source sample at a flux density level intermediate between these two is required to resolve this issue.

Taking a census of the high redshift space density of radio sources is one of the key goals of the current survey. In recent years it has become apparent that resolving this issue has far-reaching importance, since massive black holes appear to reside in all massive present-day spheroids, with a mass roughly proportional to the baryonic mass of the spheroid (Kormendy & Gebhardt 2001). This suggests that black-hole and spheroid formation are intimately linked (e.g. Richstone et al. 1998) and that understanding the cosmic evolution of black holes is of importance for testing theories of structure formation in general. There are strong indications that powerful radio activity, at least for steep spectrum radio sources (see Woo & Urry 2002 for an alternative view based on a study of flat–spectrum quasars), is only produced by the most massive black holes ($M \gtrsim 10^9 M_\odot$; e.g. Dunlop et al. 2001); the cosmic evolution of powerful radio sources may therefore offer the cleanest way to constrain the evolution of the top end of the black-hole mass function.

A complete radio source sample at these flux densities will also enable several other important astrophysical questions to be addressed. These include:

• Dual–population unification schemes of radio sources: Wall & Jackson (1997) model the radio luminosity function using just 2 parent populations of radio sources, Fanaroff & Riley (1974; hereafter FR) Class I and II, in conjunction with orientation unification. The population mix and evolution at the low luminosities of this sample will provide a critical test of this model, as well as allowing investigation of the differential evolution of FR I and FR II radio sources (c.f. Snellen & Best 2001).

• Evolution of radio source environments: studies of the environments around radio sources of different radio luminosities (e.g. Wold et al. 2000, Finn et al. 2001) show that at moderate redshifts ($z \sim 0.5$) the most luminous radio sources lie in richer environments than lower luminosity sources, in contrast to what is found in the nearby Universe (e.g. Prestage & Peacock 1988). The inconsistency of the spatial correlation functions of the Green Bank and WENSS surveys (Rengelink 1998), and the weak variation of the cross–correlation amplitude of radio sources with radio flux density (e.g. Overzier et al. 2003 and references therein) further suggest that the evolution of radio source environments may be radio luminosity dependent, in a similar manner to evolution of the comoving number densities of sources. A sample of lower luminosity sources would test this model providing valuable insight into the physical mechanisms behind radio source evolution.

• The K$-z$ relation: radio galaxies show a very tight correlation between their K-magnitude and redshift (Lilly & Longair 1984), but interestingly, the K$-z$ relations of radio galaxies from the 3CR and 6C samples, selected at different limiting radio flux densities, are in agreement at low redshifts ($z \lesssim 0.6$) but show a mean offset of ~ 0.6 magnitudes in the K-band at $z \gtrsim 1$ (Eales & Rawlings 1996; Inskip et al. 2002). This result means either that the K$-$band magnitudes of the most radio luminous sources contain a significant AGN contribution, which would have important consequences for interpretations of the spectral energy distributions of radio galaxies in terms of their stellar populations, or that more powerful radio sources at high redshift are hosted by more massive galaxies (Best et al. 1998). This second possibility is consistent with the black–hole vs spheroid mass correlation, since if the black holes in high redshift radio galaxies are fuelled at the Eddington

limit then more massive galaxies (with more massive black holes) will produce more powerful radio sources. The similarity of the K-magnitudes of the different radio samples at lower redshifts would then have interesting implications for the evolution of fuelling of these objects. Comparing the K$-z$ relation for fainter radio samples with that of the 6C sample will help to distinguish between these two possibilities (c.f. also Willott et al. 2003).

With all of these goals in mind, we have begun a project to produce a spectroscopically complete sample of ~ 150 radio sources at the $S_{1.4\,\mathrm{GHz}} \sim 10$ mJy level. This project takes advantage of two recent large surveys: the NRAO VLA Sky Survey (NVSS) which has surveyed the radio sky at 1.4 GHz, and the ESO Imaging Survey (EIS) which has provided deep optical imaging over four 3 by 2 degree fields. By combining these two surveys, a sample of radio sources can be defined for which the majority already have optical identifications for their host galaxies.

In this paper, the radio source sample is defined, the radio properties of the sample are described based on new high angular resolution observations, and a comparison of these with the EIS optical data is made. The layout of the paper is as follows. Section 2 discusses the properties (e.g. depth, size) required of a radio source sample to successfully address the question of the high redshift evolution of the radio luminosity function. In Section 3 the EIS and NVSS surveys are briefly described, together with the definition of the preliminary EIS-NVSS sample from these. The new higher resolution VLA radio observations of these sources are described in Section 4, and the radio properties of these sources are discussed in Section 5. The new radio maps are compared with the EIS optical fields in Section 6, together with a likelihood analysis to identify the possible optical host galaxies; the nature of these optical hosts is discussed. The new data are used to refine the sample definition and produce the final radio source sample, designated the CENSORS sample (a *Combined EIS–NVSS Survey of Radio Sources*), in Section 7. The results are summarised in Section 8. Subsequent papers (Brookes et al. in prep.) will present infrared K–band imaging data to identify the radio source host galaxies too faint to appear in the EIS survey, the spectroscopic follow–up observations, and the consequences of these for our understanding of the evolution of the radio luminosity function at high redshifts.

2 SAMPLE REQUIREMENTS

From the results of Waddington et al. (2001) and Jarvis et al. (2001) it is clear that to resolve the question of the redshift cut–off, what is required is near-complete redshift information for a sample selected at intermediate flux densities, $S \sim 10$ mJy. This corresponds to about the break of the radio luminosity function at redshifts $z \sim 2$; 10 mJy radio sources at redshifts $z \gtrsim 2$ are also of comparable radio luminosity to nearby luminous radio sources such as those in the 3CR sample, allowing the most direct comparison of the cosmic evolution of the intrinsic properties of the radio sources.

The suitability of the 10 mJy flux density level for radio luminosity function work is demonstrated in Figure 1, where the percentage of the radio sources in a sample above a given radio power and redshift is illustrated as a function of redshift for three different flux density limits (1, 10 and 100 mJy at 1.4 GHz), for the 'Pure luminosity evolution' model of Dunlop & Peacock (1990) with no redshift cut-off. It is clear that a 10 mJy flux density cut-off provides by far the largest fraction of powerful sources at redshifts beyond $z \sim 2$. The lower panel of Figure 1 demonstrates this further, by
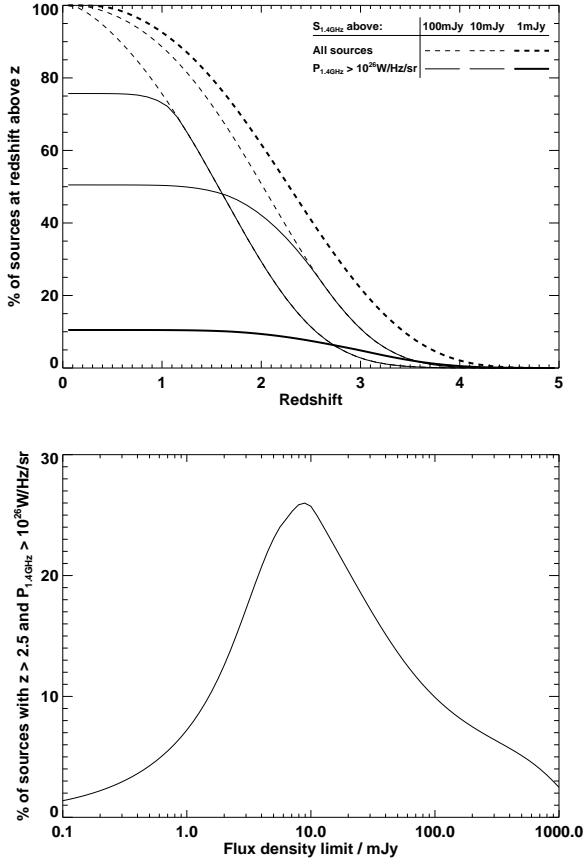
Figure 1. *Top:* The dotted lines show the percentage of sources in a flux-limited radio source sample which lie above a given redshift, for three different flux density limits (100 mJy, 10 mJy and 1 mJy, in order of increasing line thickness). The solid lines indicate the subset of those sources which have a radio power $P_{1.4\,\mathrm{GHz}} > 10^{26}\,\mathrm{W\,Hz^{-1}\,sr^{-1}}$, which corresponds roughly to the break in luminosity function. *Bottom:* The percentage of sources in a flux-limited radio source sample which have $z > 2.5$ and $P_{1.4\,\mathrm{GHz}} > 10^{26}\,\mathrm{W\,Hz^{-1}\,sr^{-1}}$, as a function of the flux density limit of the sample. All of these results are based upon the 'pure luminosity evolution' model of Dunlop & Peacock (1990), for steep-spectrum sources only, assuming no redshift cut-off. The flux densities have been converted from 2.7 to 1.4 GHz assuming a spectral index of 0.75. The Dunlop & Peacock models, which had been derived for an Einstein-de-Sitter cosmology, were converted to the currently favoured lambda cosmology ($\Omega_m = 0.3$, $\Omega_\Lambda = 0.7$, $H_0 = 65\,\mathrm{km\,s^{-1}\,Mpc^{-1}}$) using the expression provided by Peacock (1985): $\rho_1(L_1, z)\mathrm{d}V_1/\mathrm{d}z = \rho_2(L_2, z)\mathrm{d}V_2/\mathrm{d}z$, where L_1 and L_2 are the luminosities derived for a source of given flux density and redshift in the two cosmologies, V_1 and V_2 are the volumes available at a given redshift, and ρ_1 and ρ_2 are the corresponding space densities of sources. Willott et al. (2001) showed that this conversion is accurate for all regions where the data constrain the models well, although it is poorer in less-constrained regions of parameter space. The use of different evolution models will also change the precise details of these plots, but the general result that a 10 mJy flux density limit is optimal for these studies should be robust.

comparing the percentage of sources in a sample which have radio powers $P_{1.4\,\mathrm{GHz}} > 10^{26}\,\mathrm{W\,Hz^{-1}\,sr^{-1}}$ (around the break of the radio luminosity function at $z \sim 2$) and redshifts $z > 2.5$ as a function of the flux density limit of the sample. Although the exact details are model dependent, a 10 mJy sample is clearly at around

the optimal flux density level to distinguish the presence or absence of a redshift cut-off.

Another important issue, given the goal of measuring the space density of high redshift radio sources, is that the area of sky studied is large enough not to be significantly affected by large–scale structure, especially since these radio galaxies are likely to be highly clustered sources.

Clustering increases the chances of finding a galaxy at a distance r from another galaxy by a factor $\xi(r)$, such that the probability of finding two galaxies in two volumes dV_1 and dV_2 separated by a distance r is given by $P(r) = N^2[1 + \xi(r)]dV_1 dV_2$, where N is the number of galaxies per unit volume. The cross-correlation function $\xi(r)$ is known to be well–matched by a power–law, $\xi(r) = (r/r_0)^{-\gamma}$, where r_0 is the correlation length and $\gamma \approx 1.8$. Galaxies at redshifts $z \sim 3$ selected by the Lyman-break technique have been shown to have correlation lengths of $r_0 \approx 3 - 4\,\mathrm{Mpc}$ (Porciani & Giavalisco 2002). Radio galaxy hosts are likely to be more massive than these, and hence more strongly clustered; Daddi et al. (2003) find that luminous red (J−K > 1.7) galaxies with photometric redshifts $2 \lesssim z_{\mathrm{phot}} \lesssim 4$ have correlation lengths of $\sim 10 - 12\,\mathrm{Mpc}$, and these are more likely to be representative of the radio source population. At redshifts $z \sim 3$, a spatial scale of 10 Mpc corresponds to about 20 arcminutes on the sky ($\Omega_m = 0.3$, $\Omega_\Lambda = 0.7$, $H_0 = 65\,\mathrm{km\,s^{-1}\,Mpc^{-1}}$).

To assess the affect of this clustering on the high redshift radio source counts, a population of radio sources was built up, following the method outlined by Soneira & Peebles (1977; 1978), such that they had a correlation length of 12 Mpc. These were constructed over a $2000 \times 2000 \times 2000\,\mathrm{Mpc}^3$ volume. A rectangular field–of–view was then chosen, of a given long axis size (d) and a 3:2 axial ratio (to match that of the EIS Patch D – see below). The source counts were normalised to provide an average of 25 radio sources within a volume element defined by this field of view (d by $2d/3$ Mpc) and the length of the redshift interval $2.5 \lesssim z \lesssim 3.5$ ($\sim 1000\,\mathrm{Mpc}$). Then, for 100 different sight-lines through the simulation, the number of sources actually observed in this volume was determined, and this was repeated for 150 different simulations of the $2000^3\,\mathrm{Mpc}^3$ volume. This whole process was carried out for a number of different field sizes, d.

As expected, the effect of large–scale structure is to broaden the observed distribution of source counts, due to some sight–lines sampling clusters of sources and others passing through voids. The effect of clustering was quantified by measuring the width of the number count distribution, and comparing it to the Poissonian expectation. The factor by which the large–scale structure increases the distribution width (relative to Poissonian) is plotted against the field–of–view, d, in Figure 2. It is clear that for small fields clustering plays an important role, but that when the field size gets up to about 100 Mpc in size the plot begins to level off and the effect of large–scale structure has dropped below the 15–20% level. This corresponds to an angular size of about 3 by 2 degrees (at $z \sim 3$) for the survey, which is the size of the ESO Imaging Survey Patch D (see Section 3).

Finally, it is important to consider the number of radio sources required for the survey. If there is no redshift cut-off then the Dunlop & Peacock (1990) models predict that over 20% of radio sources in a sample with 10 mJy flux density limit should be at $z > 2.5$, whilst if a $z > 2$ decline is included then their pure luminosity evolution and luminosity density evolution models predict respectively ~ 9 and $\sim 5\%$ of sources above that redshift. A sample of ~ 150 radio sources is sufficient to distinguish between these possibilities at the $> 3\sigma$ level, whilst keeping the sample size to a
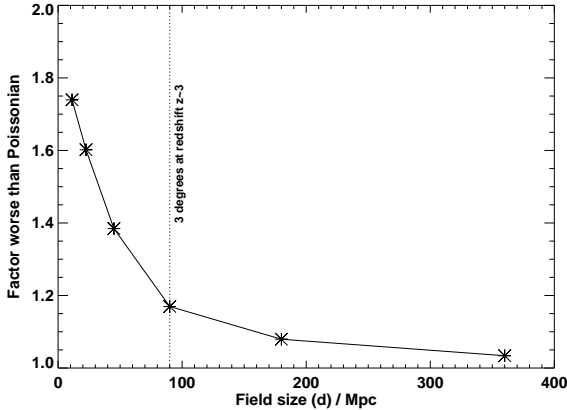
Figure 2. The effect of radio source clustering on the high redshift number counts. The plot shows the factor by which galaxy clustering increases the width of the number count distribution relative to the Poissonian expectation, as a function of field size. This is calculated by constructing a source population with a spatial cross-correlation length of 12 Mpc, normalised to have 25 sources over the field area and a unit step in redshift ($2.5 < z < 3.5$). The field area is rectangular with a 3:2 axial ratio, and the length of its longer axis (d) is shown as the abscissa. For sky areas of 3×2 degrees, the plot begins to level off and the effect of large–scale structure is below the 20% level.

manageable level. Conveniently, to obtain this number of sources down to a ~ 10 mJy flux density level also requires a sky area of order six square degrees. The combination of the EIS and NVSS surveys is therefore ideal.

3   SAMPLE DEFINITION

3.1   The ESO Imaging Survey (EIS)

The wide–field ESO Imaging Survey (EIS-wide) comprises a relatively wide–angle survey of four distinct patches of sky of up to 6 square degree each, selected to have low optical extinction and to exclude especially bright stars or nearby clusters of galaxies (Nonino et al. 1999). Of these four regions, the most northerly, Patch-D, is a 3 by 2 degree field centred at RA: 09 51 36, Dec -21 00 00 (J2000), and is thus sufficiently far north to be relatively easily accessible for radio observations with the Very Large Array (VLA) synthesis array. During the EIS-wide project, the entirety of Patch-D was imaged in the I–band using the EMMI camera mounted on the 3.5-m New Technology Telescope (NTT) at La Silla. This provides a pixel scale of 0.266 arcsec per pixel. Each region of sky was observed for 300 seconds in each of two separate exposures.

A single–entry catalogue has been constructed for the EIS Patch D in I–band (Nonino et al. 1999), in which objects detected in more than one overlapping pointing are listed as a single entry, with the parameters determined from the best seeing image; the seeing on the images ranges from 0.5 to 1.6 arcsec. This catalogue contains over 560000 objects, reaching an 80% completeness limiting I magnitude of typically $I \sim 23$ (Benoist et al. 1999). Postage–stamp images are also available. The EIS-wide survey of Patch D has been complemented by a Wide Field Imager survey (using the ESO 2.2m telescope) of the same field (see http://www.eso.org/science/eis/) in the B and V bands, reaching limiting magnitudes of $V \sim 24.5$ and $B \sim 25$. Only catalogues of each Wide Field Imager pointing are currently available, not a

combined single–entry catalogue nor postage stamp images. Astrometry on both of these surveys is accurate to within 0.2 arcsec (Nonino et al. 1999).

The B, V, and I filters used were filters designed especially for the EIS project; they have effective wavelengths close to those of the Johnson–Cousins BVI filters, but are broader and with sharper cut-offs. The transformation between the EIS magnitudes and the Johnson–Cousins magnitudes is zero for stars with colours of zero, and is significantly below 0.1 magnitudes even for objects with the most extreme colours (Nonino et al. 1999).

The extracted magnitudes used in all wavebands were derived using SExtractor (which was used to identify and measure properties of the galaxies in the EIS catalogues; for details of SExtractor see Bertin & Arnouts 1996), and are estimates of the total magnitude of the object. Note, however, that these apertures have not been precisely matched between the different catalogues, and so aperture difference will introduce some scatter into the measured colours.

3.2   The NRAO VLA Sky Survey (NVSS)

The NRAO VLA Sky Survey (NVSS) is a radio survey carried out at a frequency of 1.4 GHz using the Very Large Array in the D and DnC array configurations (Condon et al. 1998). This provides an angular resolution of about 45 arcseconds full–width at half–maximum (FWHM). The survey covers the whole sky north of $-40°$ declination (J2000), to an root–mean–squared (rms) brightness level of 0.45 mJy beam^{-1}. Thus, the survey is essentially complete to ≈ 3.5 mJy, to which level there are about 50 sources per square degree.

The 45 arcsec beam size of the NVSS survey is significantly larger than the median angular size of faint extragalactic sources at these flux density levels ($\lesssim 10$ arcsec; Condon et al. 1998), meaning that most sources will be unresolved. This has the benefit that for the majority of detected objects an individual radio source is contained within a single NVSS component, and the NVSS flux density measurement should have good photometric accuracy with little or no flux density missed by resolving out structure. However, the low angular resolution of this survey means that follow–up observations are required in order to determine the structure of a radio source, and to pin-point its position to allow identification of the optical counterpart.

3.3   Initial Sample Definition

The EIS-NVSS radio source sample was initially defined in 1997, at which stage only an early version of the NVSS catalogue had been produced, and the EIS observations were still in progress. The *original* definition of this sample was as follows:

- $09^h44^m25^s <$ RA $< 10^h00^m$
- $-22°6' <$ Dec $< -19°54'$
- $S_{1.4\,GHz} \geq 7.8$ mJy in original NVSS catalogue.

This corresponded to a sample of 199 radio sources, and these were assigned a designation of 'EISD' followed by a catalogue number which was '1' for the brightest source and increased with decreasing NVSS flux density. The sky area defined by these limits is slightly larger than the final 3×2 degree sky area of the EIS Patch D; it eventually turned out that 44 of these sources lay outside of the region covered by the optical imaging, and so are not considered in the final CENSORS sample discussed below. One source, NVSS-J095759-2005 with $S_{1.4\,GHz} = 14.9 \pm 1.1$ was found to have been

accidentally excluded from the sample. Since this lies outside of the EIS Patch D, and so is not within the CENSORS sample from which the radio luminosity function work will be carried out, this exclusion will have no significant consequences.

The sample properties differ somewhat from these initial selection criteria, since the current public NVSS catalogue (version 2.17, issued July 2002) differs substantially from the preliminary catalogue from which the observed sample was selected. Significant deviations are found in both the positions and the flux densities of the sources, suggesting that these have been re-estimated. In general, the source flux densities have been amended downwards, so that the new flux densities are on average nearly 10% lower than those originally selected, although with considerably scatter from source to source. Importantly though, some of the sources that were just below the flux density threshold in the original sample definition are now quoted to be brighter than some sources that were included in the sample. The effects of this are discussed in Section 7, and the final CENSORS sample of radio sources is defined there.

The properties of the 199 radio sources selected in the original EIS-NVSS sample are provided in Table A1 of Appendix A.

4 RADIO OBSERVATIONS

4.1 VLA BnA array observations

Radio observations of the 199 originally selected sources were taken at 1.4 GHz using the VLA in BnA configuration on 15 and 19th June 1998 (see Table A1 for details). The observations used the standard two IFs at frequencies of 1385 and 1465 MHz, with a bandwidth of 50 MHz. The BnA configuration is a hybrid between the B and A configurations with larger spacings of the antennae along the northern arm, designed to produce approximately circular beams for targets at low declinations. The angular resolution provided by this setup is typically between 3 and 4 arcseconds.

Depending on their NVSS flux densities, the sources were observed for up to 8 minutes each. The exposure time for each source was set to provide a roughly constant integrated signal–to–noise ratio of 60, for an unresolved source. For those sources with total exposure times in excess of 5 minutes, the exposure was split into two separate scans in order to improve the *uv* coverage. The primary flux calibrator 3C286 (1331+305) was observed twice during each of the runs, and was used to calibrate the flux density scale assuming flux densities of 14.55 and 14.94 Jy for that source at 1385 and 1465 MHz respectively. These are the most recently determined VLA values (1995.2), based upon the scale of Baars et al. (1977). The nearby secondary calibrator $0921-263$ was observed approximately every 30 minutes to provide accurate phase calibration.

The data were processed using standard techniques incorporated within the AIPS software provided by the National Radio Astronomy Observatory. After first applying baseline corrections and discarding data from any antenna or baseline showing excessive noise, the data were CLEANed using the AIPS task IMAGR. Maps were made over a 512 by 512 pixel field, with 0.6 arcsec pixels; to reduce the noise from the sidelobes of sources outside this central field and to obtain a good model of the field for subsequent self–calibration, the positions of all other sources within the 30 arcmin VLA primary beam with $S_{1.4\mathrm{GHz}} > 7.5$ mJy were extracted from the NVSS and 128 by 128 pixel fields centred on these positions were also included in the CLEANing process. For 193 of the sources, sufficiently bright point sources were observed within the fields that one or two cycles of phase self–calibration were used to improve further the map quality.

4.2 VLA CnB array observations

As discussed below, a number of the more extended sources were largely resolved out at the high angular resolution provided by the BnA configuration observations. For these sources, radio data at lower resolution were required. Observations of these sources (excepting EISD176 and EISD196 which lay outside the region of EIS optical imaging, and were therefore excluded due to telescope time constraints) were carried out in various observing runs during 2002 (see Table A1 for details), with integration times of typically about 5–10 minutes. Again, these observations were taken in two IFs at frequencies of 1385 and 1465 MHz, with a standard bandwidth of 50 MHz.

These CnB array data were reduced in a similar way to the BnA array data, except that in this case, due to the lower angular resolution, 1024 by 1024 pixel maps with 3 arcsec pixels were made to cover the entire primary beam. After cleaning and self–calibration, the CnB array data were combined with the BnA array data, a further cycle of self–calibration was carried out, and final images of the sources were produced using both sets of data. The resultant maps typically have angular resolutions of ~ 7 arcsec, but much greater sensitivity to extended structures that the BnA array data alone.

4.3 The radio maps

Cleaned radio maps of all of the 199 radio sources have been produced. The rms noise levels on each of these maps was calculated by taking the average of five off–source regions, and is provided in Table A1. For those radio sources within the EIS field, contoured radio maps are shown in Appendix A, in Figure A1. These maps have contour levels scaled in factors of 2 from a first contour level of three times the rms noise on the final radio map. The full–width–half–maximum of the Gaussian restoring beam is plotted in the lower left corner of each map. Contour maps of the sources which lie outside of the EIS field are shown in Figure A2, with contour levels defined in the same way. No maps are shown for those sources which are undetected in the radio waveband.

5 RADIO PROPERTIES OF THE SOURCES

5.1 Derived radio source parameters

Source characteristics were derived from the radio maps; details of all of these parameters are provided in Table A2. The AIPS task SAD (Search And Destroy) was used, which fits Gaussian models to an image by a least squares method, and estimates the errors (Condon 1997). In this way, peak flux densities (S_{peak}), integrated component flux densities (S_{comp}), and positions ($\alpha_{\mathrm{comp}}, \delta_{\mathrm{comp}}$) of all of the source components were estimated. In addition, for resolved sources the total flux density (S_{int}) was calculated by integrating all of the signal in a region surrounding the radio source; for unresolved source the integrated flux density of the single source component was adopted instead.

The source morphologies were divided into five classes: single (S), double (D), triple (T) and multiple (M) component sources, and extended diffuse sources (E). For sources with more than one component, the position angle (PA) and largest angular size (D_{rad}) of the radio source were defined as the position angle and the angular separation, respectively, of the two most separated components. For single component sources, where the component is resolved these properties were defined as the position angle and the major

Figure
3. *See attached jpeg file*. The new radio map of the EISD7 plus EISD44 combination. Radio contours are at (-1,1,2,4,8,16,32,64,128,256,512,1024) $\times$ 66 μJy beam^{-1}. EISD7 is an unresolved radio source, whilst the other radio components make EISD44.

axis length of the deconvolved elliptical Gaussian fit to the component. For sources with a single unresolved component, the position angle was not determined, and a 1σ upper limit to the largest angular size was derived from the upper limit to the major axis of the deconvolved elliptical Gaussian fit.

5.2   Notes on individual radio sources

EISD7: This source appears double with EISD44 in the NVSS catalogue. The new radio map (Figure 3) indicates that EISD7 is indeed a bright unresolved radio source, close to the position of its entry in the NVSS catalogue. EISD44 is an extended radio source, stretching nearly 2 arcminutes on the sky, and therefore its NVSS catalogue position and flux density are both inaccurate.

EISD15: The weak second radio component, 25 arcsec south-south-east of the central component, is probably unconnected with this source.

EISD16: This source overlaps with sources EISD56 and EISD114, and a source below the 7.5 mJy flux density limit in the NVSS catalogue (Figure 4), and it is not entirely clear from the radio data alone which radio components comprise which distinct sources. Addition of the optical data (see Section 6) clears this up a bit, but not entirely (Figure 4). It is clear that the radio components labelled 'A' on the figure correspond to an extended double radio source, associated with EISD16. Component 'F' is the weak radio point source seen in the NVSS map, and has an associated optical counterpart. Component 'D' also has an optical counterpart, and causes the apparent extension of EISD56. The complication arises with components 'B', 'C' and 'E'. These may be simply interpreted as three separate radio sources, of which 'B' and 'E' correspond to EISD114 and EISD56 respectively, and 'C' is a radio point source below the sample limit; this component 'C' also has an optical identification. However, the facts that neither component 'B' nor 'E' has an optical counterpart, that 'C' lies almost midway between the two, and that component 'B' apears to be slightly extended, pointing towards 'C', suggests an alternative explanation whereby these all form one giant radio source with 'C' as the core. The lack of extended radio emission between the two in the NVSS map argues against this, and in favour of the three radio source model; in the absence of evidence to the contrary, this simple solution is adopted in the subsequent sample definition. However, deeper radio observations will be required to elucidate exactly which components constitute independent sources.

EISD20: The NVSS entry for EISD20 corresponds to the bright unresolved radio component to the south of the radio map in Figure A1. The further two components to the north appear as a separate NVSS entry, whose flux density is too low to make it into the EIS–NVSS sample. Although it is possible that these three comprise a single extended radio source, the large flux density ratio between the two lobes in this cases, coupled with the unresolved nature of the southern radio component, make this unlikely. More likely, the unresolved component in the south is indeed EISD20, as defined from the NVSS, whilst further north there's a weak double hosted by the optical counterpart at 09 54 27.8, -21 56 27.

Figure 5. *See attached jpeg file*. A contour representation of the NVSS map of EISD25 and EISD86, whose locations are labelled by crosses, overlaid on a greyscale image of the new radio data. NVSS radio contours are at $(-1,1,2,4,8,16,32,64,128) \times 1.5$ mJy beam^{-1}. The two NVSS sources appear to arise from a misfit to the NVSS data, due to the faint extension to the south–west. The new radio data confirm this, with no emission detected at the location of EISD86.

EISD24: The additional two radio components to the south are most likely an unassociated double radio source.

EISD25: In the NVSS catalogue, the sources EISD25 and EISD86 appear separated by less than 10 arcseconds. Figure 5 shows that these two NVSS sources result from a misfit to a single bright source with a faint extension. The BnA array data clearly show that this is a single source, located at the peak of the NVSS flux.

EISD38: The radio structure of this source is very unclear. A narrow double is seen, together with a faint third component 25 arcsec further north. The relationship between these components is unclear. The position angle and largest size of the radio source were derived considering only the southern components.

EISD44: See comment on EISD7.

EISD56: See comment on EISD16

EISD73: EISD73 lies in an extended NVSS structure associated with EISD151 and EISD103. Nearby on the sky, EISD77 is another extended NVSS structure close to the source EISD112. These five radio sources are shown in Figure 6. It is noteworthy that the two extended regions of emission in the NVSS map are both oriented in the same direction, and that for none of these three NVSS sources is any radio counterpart seen in the new CnB or BnA images. Whilst it cannot be stated with 100% confidence that these sources do not represent extended emission, perhaps associated with an FR I radio source, the failure to detect signal even in the CnB array data, and the absence of a bright galaxy which might host such a radio source, both argue against this. Further, the false source EISD118 (see below) is also found nearby, and has similar orientation. These results strongly suggest that the three sources associated with the extended NVSS emission regions (EISD73, 77 and 151) are not real, but instead are caused by correlated noise associated with bad baselines or calibration errors in the NVSS data of that pointing. These three sources are therefore removed from the final catalogue.

EISD77: See comment on EISD73. This source is not real and is therefore removed from the final catalogue.

EISD86: See comment on EISD25. This source is not real and is therefore removed from the final catalogue.

EISD90: See comment on EISD113.

EISD98: The weak second lobe to the north of this source is very diffuse, but is believable because it provides consistency between the observed position and that in the NVSS catalogue. The NVSS catalogue position also coincides almost exactly with the position of a very bright optical galaxy.

EISD103: See comment on EISD73

EISD112: See comment on EISD73

EISD113: The BnA radio map of this source has an odd morphology. This source was also observed off–axis in the CnB observations of EISD7 and 44, although with significant primary beam attenuation. These lower resolution observations confirm the two components extracted here (see Figure 7). However, it is also noticeable that this radio source lies close on the sky to EISD90, and it cannot be excluded that these two form a single extended radio source. The lack of further extended emission between the two and the compact nature of the EISD90 radio source, with a potential optical identification, argue against this. The two sources are therefore

Figure 4. *See attached jpeg file.* Upper left: the NVSS map of EISD16, EISD56 and EISD114; radio contours are at $(-1,1,2,4,8,16,32,64,128) \times$ $1.5 \, \text{mJy beam}^{-1}$. Upper right: the new radio map produced by combining the CnB and BnA array data for this field, overlaid upon the EIS I–band image. Radio contours are at $(-1,1,2,4,8,16,32,64,128,256,512,1024) \times 84 \, \mu\text{Jy beam}^{-1}$. Six different components of radio sources are labelled; see text for discussion. Lower panels: postage-stamp enlargements of the three components C,D and F (from left to right), demonstrating the relaity of their optical counterparts.

Figure 6. *See attached jpeg file.* A contour respresentation of the NVSS radio map of the EISD73, EISD77, EISD103, EISD112 and EISD151, with radio contours at $(-1,1,2,4,8,16,32,64,128) \times 1.5 \, \text{mJy beam}^{-1}$. Overlaid on this is a greyscale image of the new BnA radio data. The apparent extended emission associated with EISD73, EISD77 and EISD151 is due to correlated noise on the NVSS map. Note that the CnB array data (more sensitive to larger scale structure) also shows no evidence for extended emission associated with these three sources.

Figure 7. *See attached jpeg file.* A contour respresentation of the off–axis CnB array radio map (corrected for primary beam attenuation) of EISD113 and EISD90. Contour levels are at $(-1,1,2,4,8,16,32,64,128) \times$ $200 \mu\text{Jy beam}^{-1}$. The I–band EIS image is overlaid in greyscale.

Figure 8. *See attached jpeg file.* A contour respresentation of the NVSS radio map of EISD118, EISD11 and EISD29, with radio contours at $(-1,1,2,4,8,16,32,64,128) \times 1.5 \, \text{mJy beam}^{-1}$, and a greyscale image of the new BnA radio data overlaid. EISD118 is associated with an extended stripe of emission, with no counterpart in the BnA array data, indicating that this source is not real.

considered separately in this paper, although further radio observations will be required to confirm this.

EISD114: See comment on EISD16

EISD118: No radio source was detected. As shown in Figure 8, this NVSS source appears to be just a residual close to the bright sources EISD11 and EISD29, due to calibration and/or cleaning errors. This source also lies close on the sky to the EISD73–77–103–112–151 region, where the problems discussed above under EISD73 are found, further confirming that this source is not real. It is therefore removed from the final catalogue.

EISD124: EISD124 and EISD137 are closely separated sources in the NVSS catalogue, and the new radio maps (Figure 9) show clearly that EISD137 is an unresolved source associated with a bright nearby galaxy, whilst EISD124 stretches over 2.5 arcminutes top to bottom. The northern component of EISD124 is unresolved from EISD137 in the NVSS image, and thus the positions and locations of these two sources are poorly described by their NVSS catalogue entries.

EISD137: See comment on EISD124

EISD151: See comment on EISD73. This source is not real and is therefore removed from the final catalogue.

EISD163: This radio source was only weakly detected in the BnA array observations, suggesting an extended radio source. Because the optical images showed this to be clearly associated with a very nearby galaxy, more detailed CnB radio data were not taken. For clarity, the NVSS contours are used instead of the new BnA array data in the radio–optical overlay.

EISD176: This radio source was undetected in the BnA array observations but, because it lies outside the field of the optical imag-

Figure 9. *See attached jpeg file.* The new radio map of the EISD124 plus EISD137 combination, overlaid upon the EIS I–band image. Radio contours are at $(-1,1,2,4,8,16,32,64,128,256,512,1024) \times 54 \, \mu\text{Jy beam}^{-1}$. EISD137 is an unresolved radio source, whilst the other radio components make up northern and southern lobes of the extended source EISD124.

ing, was not followed up in CnB array observations. It is likely to be a significantly extended radio source.

EISD191: As EISD163.

EISD196: As EISD176.

5.3 Radio source properties

The radio flux densities of the EIS sources as determined in the new radio observations are compared to the values in the NVSS catalogue in Figure 10. To make this comparison, the newly determined flux densities were scaled up by $\sim 1.5\%$ to account for the small difference between the mean radio frequency of the current observations (1425 MHz) and those of the NVSS (1400 MHz), assuming a typical radio spectral index of $\alpha \approx 0.75$ (where $S_\nu \propto \nu^{-\alpha}$). It can be seen that in addition to the scatter in the ratio of the two flux densities, arising from the uncertainties in the two sets of measurements, there is also a tendency for the new observations to determine a lower flux density than suggested by the NVSS.

Sources which are in the brighter half of the sample, so that they are detected at high signal–to–noise in both sets of observations, and which are also unresolved, so that no flux should be lost in the current high resolution observations, are indicated by filled circles in Figure 10. The NVSS flux densities of these are on average 2–3% higher than those of the new observations, which can be attributed to calibration errors between the two different sets of observations. The flux densities scatter by of order 10%, suggesting that the true uncertainties in the flux densities are slightly higher than the formal errors in at least one of the two sets of measurements. For fainter and extended sources (open circles in Figure 10) the average ratio is around 0.8 to 0.85, with larger scatter; Figure 11 demonstrates that the average flux ratio is lower for sources with larger angular sizes, indicating that to at least some extent this difference in flux densities is due to extended emission being resolved out at the higher angular resolution of the new observations. The NVSS flux densities, despite their larger uncertainties, probably give a more accurate guide to the total flux densities of the extended sources.

The distribution of radio source morphologies across the five different morphological classes defined above is indicated in Table 1. Fractionally over half of the sources are classified as single component sources; this proportion rises to 60% for the fainter sources (EISD101 to EISD199), whilst the proportion of triple and multiple sources drops from 16% for the brightest 100 sources to 7% for the fainter half of the sample. This implies that at fainter radio flux density levels, a larger fraction of unresolved radio sources are being picked out.

There is a possible concern that this results stems from second faint radio components being missed for fainter radio sources, due to the relatively low signal–to–noise of current the observa-
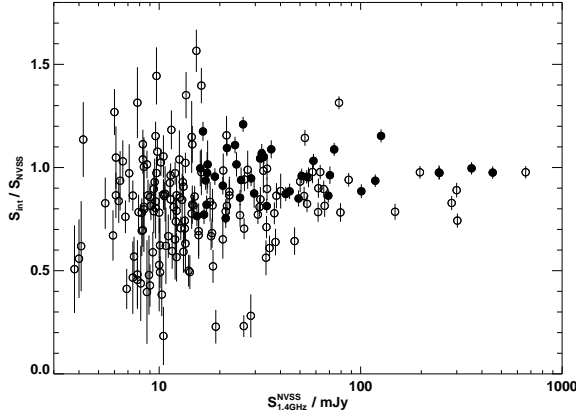
Figure 10. The ratio of the 1.4 GHz flux density determined for the EIS sources in the new radio observations compared to the NVSS catalogue, as a function of radio source flux density. Note that the new radio flux densities have been increased by 1.5% in this plot, to account for the small frequency difference (1425 MHz compared to 1400 MHz) of the current observations compared to the NVSS, assuming a mean spectral index of 0.8. The filled circles represent the single–component radio sources between EISD-1 and EISD-100, and the open circles are all fainter than this, or extended sources.
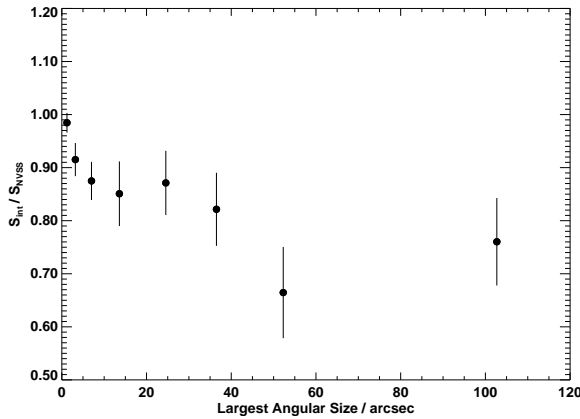
Figure 11. The median ratio of the 1.4 GHz flux density determined for the EIS sources in the new radio observations compared to the NVSS catalogue, as a function of the angular size of the radio source, for 8 bins in angular size. The lower values for sources with larger angular extents implies that some extended emission is being resolved out in the new radio observations.

tions; it was shown above that extended emission is often missed, and diffuse emission from an FR I source will also be hard to detect. However, it is already well-known that fainter radio sources tend to have smaller projected angular sizes (cf. Oort et al.1987, Neeser et al.1995), for example, the median projected angular size of the revised 3CR sample ($\sim$ 100 times brighter in flux density that the current sample) is 43 arcsec, while that of the 6C sample (a factor of $\sim$ 5 fainter than 3CR) is only 14 arcsec (Eales 1985b). The distribution of projected angular sizes of the EIS-NVSS radio sources is provided in Figure 12: the median projected angular size is found to be 6 arcsec, consistent with the above trend. In terms of multi-component nature, less than 10% of the 3CR radio sources would be unresolved at the resolution of the current observations (Laing et al. 1983), but in the Hubble Deep Field observations of Richards et al. (1998), which reach about a factor of 100 deeper

Table 1. Distribution of radio source morphologies

Source structure		Number of sources		
		All	EISD1-100	EISD101-199
Single	(S)	101	42	59
Double	(D)	66	39	27
Triple	(T)	17	11	6
Multiple	(M)	6	5	1
Extended	(E)	2	0	2
Undetected/False		7	3	4
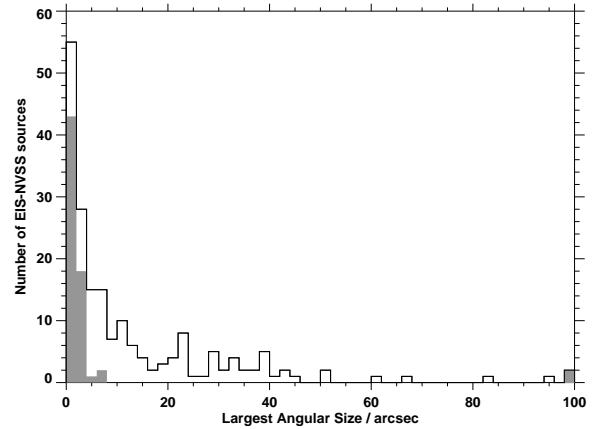
Figure 12. The distribution of projected angular sizes of the EIS-NVSS radio sources. The shaded regions represent upper limits to the unresolved radio sources, and those sources whose angular sizes are larger than 100 arcsec.

than the current sample, at least 25 of the 29 sources would be classified as single component sources. The fraction of single component sources observed within the EIS sample, and the trend with radio flux density, are both therefore consistent with these results. This indicates that whilst there is a legitimate concern that a small number of faint radio components may be missed, this should not dramatically bias the properties of the sample as a whole.

An additional radio feature which is striking in some of the radio sources is the dramatic difference in integrated flux density between the two different lobes of the radio source. In cases such as EISD30 and EISD55, one lobe is more than 20 times brighter than the other. In Figure 13 the flux density ratios of the brighter to the fainter lobe are displayed for those EIS-NVSS sources where the two lobes could be clearly defined; the median flux density ratio is 1.7, with quite a long tail towards large asymmetries. However, this feature is not unique to this sample, nor indeed to lower power radio sources. McCarthy, van Breugel & Kapahi (1991) investigated asymmetries in the 3CR sample, and their results (for radio galaxies and quasars combined) are also shown on Figure 13. Although at a slightly higher radio frequency (5 GHz), which may enhance beaming effects and therefore increase asymmetries fractionally, it is clear that a comparable range of asymmetries are seen in the 3CR sample as in the EIS-NVSS sample. The median flux density ratio of the 3CR samples is slightly smaller, at 1.5, and there are fewer sources with extreme asymmetries, but the differences between the two samples are not statistically significant. It appears that there is little correlation between lobe flux density asymmetries and the flux density of the radio source. A more detailed investigation of
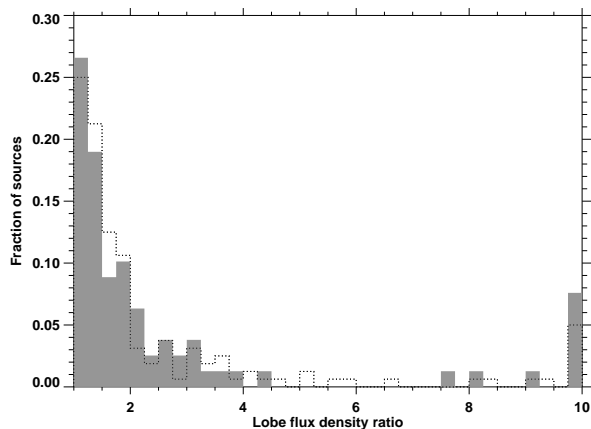
Figure 13. The distribution of flux density ratios of the brighter to the fainter lobe for those EIS-NVSS radio sources in which lobes could be clearly defined (shaded histogram), compared to the equivalent values for the 3CR sample (dotted histogram). The latter values are taken from McCarthy et al. (1991). The final bin contains all sources with flux density ratios in excess of 10.

this property, and investigation of further radio source asymmetries such as differences in the lobe lengths, and bending angles of the sources, must await the completion of the host galaxy identifications of the sources.

6 OPTICAL COUNTERPARTS

6.1 Radio–optical overlays

3 by 3 arcminute I–band images around each of the radio sources were retrieved from the EIS data archive. These co-added images use the conical equal area projection (COE; e.g. Greisen & Calabretta 2002) around the centre of the EIS Patch D at $\alpha = 147.00$, $\delta = -21.00$, in order to produce equal area pixels with minimal distortion over the large 3 by 2 degree field. The COE projection is not supported by most data reduction packages; it was therefore locally approximated by the standard TAN projection by determining the exact pixel position on the image cut-outs appropriate for the right ascension and declination of the radio source, and adjusting the FITS headers so that the TAN projection gave the correct astrometry at this position. However, the TAN projection approximation is only precise at the position of the radio source: the offset between the TAN projection approximation and the true position in these image cut-outs will increase with distance from the radio source, reaching nearly a 1 arcsecond error at radial distances of an arcminute. This is not important since in general only the region at the very centre of the field around the radio source is of interest, and in any case all optical positions were determined directly from the EIS catalogue, where they are precisely calculated from the COE projection.

For all of the true radio sources which are within the EIS field, I–band optical overlays are presented on the radio maps in Figure A1.

6.2 Identification likelihood ratios

To investigate possible optical counterparts to the radio sources, a likelihood analysis was carried out on the I–band catalogue. This was carried out in two different ways. For single radio component

sources, or those in which a clear radio core is visible on the images, a simple likelihood analysis based on the relative positions of the optical galaxies and the radio position was carried out. This likelihood ratio technique (e.g. Richter 1975, de Ruiter et al. 1977) can be used to statistically investigate whether a proposed optical identification is the real counterpart of a radio source, and is summarised in Appendix B. For extended sources with no clear radio core, a modified likelihood analysis was performed to account for the much greater uncertainty in the position of the radio source. In this technique, the distribution of lobe arm–length ratios and lobe bending angles for the 3CR sample (e.g. Best et al. 1995) is used to provide a further prior on the expected host galaxy position, and included in the likelihood analysis; this technique is also described in Appendix B.

Details of the optical host candidates which had a likelihood ratio above the cut-off for each of these two analysis are presented in Table B1. A further two classes of optical candidates were also added to this table. The first of these are very bright host galaxies which were either excluded from the EIS catalogue due to saturation, or were so large that the EIS catalogue position is inaccurate leading to a low likelihood ratio. The second class of added host candidates are optical galaxies which lie directly on top of an unresolved "lobe" of extended radio sources, which would have a likelihood ratio in excess of the cut-off if that radio component were deemed to be the radio core. These were included due to the possibility that this unresolved component is actually the AGN location, and the radio source is either one–sided or a fainter second lobe has been missed in the new radio observations. The selection method by which each optical host candidate is included is noted in the table. In total, 102 of the 150 detected radio sources within the EIS optical imaging field have likely optical identifications. For the remainder, either the true optical host is detected but the radio source is highly asymmetric and the identification falls below the likelihood cut–off threshold, or the host galaxy is too faint to be detected to this optical imaging depth.

For each of the 102 selected optical hosts, the B and V band catalogues were searched for corresponding matches, and magnitudes of the host galaxies in these bands, where detected, are presented in Table B1. Also presented in that table for each optical host is the 'stellaricity' (S/G) of the host galaxy in the I–band. This is a parameter measured by SExtractor (Bertin & Arnouts 1996) to help distinguish between stellar (or quasi–stellar) and extended objects: unresolved objects are assigned a stellaricity value of 1.0, and clearly resolved objects a value of 0.0, with the range of values in between providing a likelihood estimate in uncertain cases.

6.3 Notes on individual optical host galaxies

EISD3: In the EIS I–band catalogue the two central objects erroneously appear as a single entry at 09 50 31.32, -21 02 44.4 with a magnitude of 20.15. In the other two bands they appear as two separate objects. The optical position was taken from the V–band data, and the I–band magnitude was re-determined.
EISD6: Two potential optical counterparts are found to this extended radio source. These have similar likelihood ratios, with the brighter galaxy to the north marginally favoured.
EISD16: Although there is a weak radio feature towards the centre of this radio source, it is not clear if this is a core. A likelihood analysis treating the source as an extended source picks out the unresolved object associated with a radio structure to the north as the most likely optical counterpart.

EISD38: The $I \sim 19$ galaxy lying exactly on the south–eastern radio component is selected as a potential host galaxy.

EISD41: There are two optical objects identified between the radio lobes, but neither achieves a likelihood ratio in excess of the cut-off.

EISD47: This candidate should be considered very tentative, owing to the extremely faint I–band magnitude.

EISD60: The faint optical object associated with the western radio component is kept as a potential id.

EISD87: There are many optical galaxies close to the radio position, but none achieves a likelihood ratio above the cut-off value.

EISD91: The two optical objects near the centre of the radio source are blended into a single object in the I–band catalogue. In the other two bands they appear as two separate objects. The optical position was taken from the V–band data, and the I–band magnitude was re-determined.

EISD102: The luminous galaxy coincident with the southern radio component is retained as a likely optical counterpart.

EISD110: Strangely, this bright optical galaxy is not found within the EIS I–band catalogue, although it is in the V and B band catalogues. Its I–band magnitude was measured directly from the image.

EISD120: The faint extended emission seen in the I–band overlay is not catalogued within the EIS catalogue, but appears convincingly on the image and so its magnitude and position have been determined.

EISD123: This bright saturated galaxy is excluded from the EIS catalogue, but is clearly the optical counterpart to the radio source. The optical image shows it to be part of a merging system, with numerous bright tidal features, including a long tidal tail stretching to the north.

EISD148: The $I \sim 19$ object coincident with the eastern radio component is considered a likely optical id.

EISD155: There is a bright galaxy overlying the northern radio component, which is identified as a likely counterpart.

EISD162: The likely radio source counterpart is a fainter object close to a brighter star. Although clearly distinct, these two objects are not separated in any of the three catalogues. In the I–band the position and an estimate of the magnitude of the source were determined from the image.

EISD163: This very bright saturated galaxy is not included in the optical catalogue. Also known as ESO 566-G 014, it has a redshift of 0.01559 in the NASA/IPAC Extragalactic Database (NED). Its magnitudes quoted there are $B = 14.9 \pm 0.1$, $R = 14.0 \pm 0.1$ and $I = 13.7 \pm 0.1$.

EISD171: Two plausible optical counterparts are picked out by the likelihood analysis, although in fact there are several I–band objects close to the radio lobes, the majority of which (including the two selected candidates) appear to be unresolved. It is not clear whether either of these is really a good candidate.

EISD178: The galaxy close to the south–western radio lobe is retained as a plausible optical host.

EISD181: This candidate should be considered very tentative, owing to the extremely faint I–band magnitude.

EISD191: This very bright nearby spiral galaxy has a redshift of $z = 0.02935$ in NED, but in the EIS imaging is saturated and excluded from the catalogue. The galaxy is also known as ESO 566-G 018, and has colours from NED of $B = 14.1 \pm 0.1$, $R = 13.1 \pm 0.1$ and $I = 12.7 \pm 0.1$.

6.4 The optical hosts

The distribution of I–band magnitudes of the galaxies selected as likely optical counterparts to the radio sources is shown in Figure 14. For 48 radio sources, no optical counterpart with a sufficiently high likelihood ratio was found, and so these are not represented on this plot. It is likely that the majority of these lie fainter than the $I \sim 23.5$ magnitude limit of the EIS observations, but some may be brighter host galaxies which are detected in EIS but do not have sufficiently high likelihood ratios, for example due to highly asymmetric radio sources.

The I–band magnitudes can be used to provide a first estimate of the redshift distribution of the radio sources[†]. This is because powerful radio sources are invariably hosted by giant elliptical galaxies with a narrow spread of absolute magnitudes, and hence their magnitudes and redshifts are tightly correlated. These correlations show least scatter at near–infrared wavelengths (e.g. the $K - z$ relation; Lilly & Longair 1984)(1984) where the emission is dominated by that of old evolved stars, even at redshifts $z \sim 1 - 2$, and so any on–going low–level star formation or emission associated with the active nucleus have lesser effect.

Magnitude–redshift correlations are also found at optical wavelengths (e.g. Eales 1985c) although these have more scatter, particularly for powerful radio galaxies at high redshifts. This is because powerful radio galaxies with redshift $z \gtrsim 0.6$ display considerable excess blue emission aligned along their radio axes, due to AGN–related activity or recent star formation (the alignment effect; McCarthy et al. 1987, Chambers et al. 1987). The use of an $R - z$ or $I - z$ relation for 3CR sources beyond that redshift is therefore not appropriate for the EIS–NVSS sources, which are expected to be much more passive because the strength of the alignment effect is strongly correlated with radio power (Inskip et al. 2003). Gigahertz–peaked spectrum (GPS) sources, however, show no strong alignment effect, and so their optical magnitude versus redshift relation may provide a good approximation to that of the EIS–NVSS sources. Snellen et al. (1996) find that the $r - z$ relation of GPS radio galaxies can be roughly parameterised as $r = 22.7 + 7.4 \log z$.

Magnitude–redshift relations only hold for the radio galaxies, and so the quasars must be removed from the sample. Table B1 gives the BVI colours of the optical candidates, and an estimate of the star–galaxy classification of these in the I–band, using the SExtractor stellaricity estimator provided in the EIS catalogue. This estimator gives a value ranging between 0 (for galaxies) and 1 (for stars). Of the 102 optical counterparts, the 12 with a stellaricity S/G> 0.9 were classified as likely quasars, as were the further two objects with stellaricities S/G> 0.6 and colours $B - I < 1.0$, since distant galaxies are unlikely to have colours this blue (the other objects with $0.6 <$S/G< 0.9 all had colours $B - I > 1.8$, so the exact choice of colour cut-off is not critical). Note that this fraction of quasars ($\sim 14\%$) is much lower than the $\sim 30\%$ found in the brightest radio source samples (e.g. Best et al. 1999), although some fainter quasars may have been misclassified as galaxies if their signal–to–noise is too low to allow good differentiation.

[†] This method is preferred to using the 3-colour information to obtain photometric redshifts, because on comparison with our existing spectroscopic data (Brookes et al. in preparation) it is found to be more reliable, even when the template models in the photometric redshift estimation are restricted to only passive ellipticals. This is undoubtedly due to the small number of available colours, the fact that apertures are not explicitly matched, and the generally large uncertainties on the B-band magnitudes.
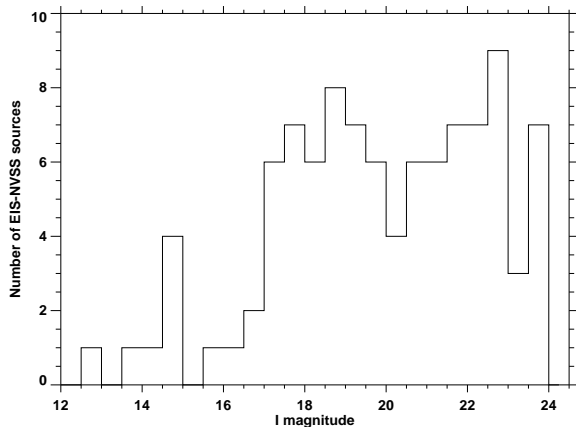
Figure 14. The distribution of I–band magnitudes of the objects selected as likely optical counterparts of the EIS-NVSS radio sources. The 48 radio sources without a sufficiently likely optical counterpart are not represented on this plot. The majority of these are likely to be undetected in the EIS imaging, and hence have $I \gtrsim 23.5$, but some may simply be asymmetric radio sources for which the true host is optically detected but is not selected as having a sufficiently high likelihood ratio.

Figure 15. The estimated redshift distribution of the 89 radio sources with optical identifications that are not associated with suspected quasars. This redshift distribution is based solely upon the I–band magnitudes (see text for details). As in Figure 14, the 48 radio sources without a sufficiently likely optical counterpart are not represented on this plot. The majority of these will be optically undetected to $I \sim 23.5$, and hence have estimated redshifts $z_{\rm est} \gtrsim 1.75$.

The I–magnitudes of the radio galaxy hosts were converted to r–magnitudes using the K and evolutionary corrections of Poggianti (1997), for an elliptical galaxy which formed at high redshift with an exponentially decreasing star formation rate of e–folding time of 1 Gyr. These were then used to provide a redshift estimate using the parameterised $r - z$ relation above. Such conversions are undoubtedly uncertain at the ± 0.2 magnitude level, but are accurate enough to allow rough redshift estimation and hence a first look at the redshift distribution of the EIS–NVSS sources. The estimated redshift distribution is shown in Figure 15. Again, the 48 sources with no acceptable optical identification are excluded from this plot (as are the quasars for which redshift estimation was not possible). A large proportion of these 48 unidentified sources are likely to have $I \gtrsim 23.5$, and hence lie at redshifts $z \gtrsim 1.5 - 2$. Over a third of the EIS-NVSS sources are therefore estimated to lie at high redshifts, $z \gtrsim 1.5$; spectroscopic measurements are clearly required, but this sample should indeed prove ideal for investigation of the reality of a high redshift decline of the space density of powerful radio sources.

7 THE CENSORS SAMPLE

7.1 Sample definition

As discussed in Section 3, the flux densities of the sources in the NVSS catalogue have been re-estimated since the original sample was defined. In addition, 44 of the EIS–NVSS radio sources lie outside of the EIS Patch D, five of the NVSS sources within the optical imaging region have been shown to be false, and some extended radio sources extend over more than one NVSS component. These facts require a re–definition of the final sample of radio sources for further study, which hereafter is referred to as the *CENSORS* sample (*A Combined EIS–NVSS Survey Of Radio Sources*)[‡]

[‡] Note that this CENSORS numbering system was not used from the start of this paper, because the EIS–NVSS numbering system is that which corresponds to the VLA radio observations in the archive, and also to the majority

150 of the observed radio sources satisfy the criteria of the CENSORS sample, namely being confirmed radio sources within the EIS imaging area, and the new sample is defined in Table C1, in Appendix C. These sources are ordered in order of decreasing flux density in the latest version (v2.17) of the NVSS catalogue, with adjustments to these values being made for five sources, marked with asterisks, due to their overlap with other NVSS sources: for EISD7 and EISD137, the flux densities of the point sources are accurately determined from the new observations, converted to a 1.400 GHz flux density assuming a spectral index of 0.8, and the NVSS flux density not accounted for in these point sources is assigned to EISD44 and EISD124 respectively. For EISD56 the flux density is calculated excluding the contribution from the nearby point sources. The median 1.4 GHz flux density of the CENSORS sample is ≈ 15 mJy.

7.2 Sample Completeness

The revision in the NVSS flux densities means that there is now a tail of sources with low flux densities. Considering the most recent NVSS catalogue, the CENSORS sample includes all of the radio sources brighter than $S_{1.4\,{\rm GHz}} = 7.2$ mJy, together with additional fainter sources. Further, only three sources brighter than 6.5 mJy were not targeted in the original EISD radio observations, these being NVSS-J094651-2125 at $S_{1.4\,{\rm GHz}} = 7.2$ mJy, NVSS-J095233-2129 at 6.8 mJy and NVSS-J095240-2123 at 6.7 mJy. All three of these sources lie well within the primary beam of the radio observations of a different EIS–NVSS source, and so radio data are available in each case. Their radio–optical overlays are shown in Figure A3, and their properties are included in Table C1 as CENSORS-X1 to X3. Including these three sources in the CENSORS sample makes it complete for all NVSS sources brighter than $S_{1.4\,{\rm GHz}} = 6.5$ mJy, with 9 additional sources below this limit.

Another recent development is that Blake & Wall (2002)

---

of the infrared and spectroscopic follow–up (Brookes et al. in preparation), and hence will be required for archive researchers.

showed that about 7% of all radio sources are resolved into multiple components by NVSS. This multiple–component effect is seen within the NVSS sources selected in the current sample, as discussed above. However, it is clearly also important to consider whether radio sources which should be above the flux density limit have been excluded from the sample due to being split into different NVSS components, each of which fell below the flux density limit. This was tested in two ways. Firstly the entire NVSS map of the EIS field was eyeballed to search for potential extended sources with more than two NVSS components, or of physical extent in excess of 3 arcminutes. No promising candidates were found (it should be noted that Lara et al. (2001) estimated that only 1 in 10000 NVSS radio sources are larger than 3 arcmins in size, and so in a small field like this, none would be expected). Secondly, using the NVSS catalogue of this region, a search was made for all NVSS source pairs separated by less than 3 arcminutes, where the two NVSS sources were both fainter than 6.5 mJy but the combined flux would put them in to the sample. From the results of Blake & Wall (2002) about 15% of all pairs with 3 arcmin separations are expected to be true double sources, rising to nearly 50% at 2 arcmins, and the vast majority of smaller separation doubles.

Only two NVSS pairs not already included in the sample were found with separations below 2 arcmins. One of these is clearly two distinct radio sources, since one of the sources has a bright optical counterpart. For the other, neither NVSS source has a clear optical counterpart, but one of the NVSS sources appears off-centre in one of the BnA radio maps, and appears unresolved. Also, there is no evidence in the NVSS map for any extension between the sources. Therefore it appears that both of these two pairs are chance alignments. A further 6 NVSS source pairs are found with separations between 2 and 3 arcmins. Three of these can be excluded as doubles on the basis of the radio and optical data; a further two are ambiguous, with no bright optical identifications for either NVSS source, but insufficient positional accuracy to rule out faint counterparts. However, these have no apparent extensions in the NVSS, no obvious bright candidate host galaxy between the two radio lobes (the majority of large angular separation radio sources have relatively low redshifts), and flux density ratios $\gtrsim 2$ between the two NVSS sources, and so are unlikely to be double radio sources. These source pairs are therefore not considered further. The final NVSS source pair, however, NVSS-J095218-2038 and NVSS-J095223-2041 with flux densities of 3.6 and 3.8mJy and a separation of 2.8 arcmins, provide a promising candidate (cf Figure A3). These sources show extensions in the NVSS indicative of a possible double, have a flux density ratio close to unity, have no obvious optical counterparts individually, but have an $I \sim 22$ galaxy situated roughly midway between them. This pair is therefore provisionally added to the final sample (called CENSORS-D1) as a possible large double.

8   CONCLUSIONS

A new sample of ~ 150 radio sources has been defined by combining the NVSS radio survey with the EIS optical observations over a 3 by 2 degree patch of sky. The median radio flux density of these sources is $S_{1.4\,\mathrm{GHz}} \sim 15\,\mathrm{mJy}$, corresponding to a factor of a few lower flux densities than existing samples of radio sources with complete redshift information. These sources are selected at an ideal flux density limit to carry out a census of the high redshift space density of radio sources, and specifically to investigate the reality of a high redshift cut–off in the radio luminosity function.

It is shown that the field studied is large enough that the effects of radio source clustering will not dominate the results.

High resolution VLA radio observations have cleared up ambiguities in the radio selected sample and provided accurate positions and morphologies for these sources. The median radio size of the sources is 6 arcsec, and approximately half of the sources appear as single radio component sources; these results are in line with the trend for lower flux density radio sources to be typically less extended. The lobe flux ratio asymmetries of the sources are comparable to those of the brightest radio sources.

Comparison with the EIS optical imaging has allowed optical counterparts to be identified for over two–thirds of the radio sources. Estimated redshifts for these sources, based upon their optical magnitudes, suggest that over a third of the galaxies lie at redshifts $z \gtrsim 1.5$ confirming the interest in spectroscopic follow–up of this sample. Infrared imaging to identify the remainder of the sample and the results of spectroscopic follow–up observations will be presented in subsequent papers.

REFERENCES

Allington-Smith J. R., 1984, MNRAS, 209, 665
Baars J. W. M., Genzel R., Pauliny-Toth I. I. K., Witzel A., 1977, A&A, 61, 99
Benoist C., da Costa L., Olsen L. F., Deul E., Erben T., Guarnieri M. D., Hook R., Nonino M., Prandoni I., Scodeggio M., Slijkhuis R., Wicenec A., Zaggia S., 1999, A&A, 346, 58
Bertin E., Arnouts S., 1996, A&A Supp., 117, 393
Best P. N., Bailer D. M., Longair M. S., Riley J. M., 1995, MNRAS, 275, 1171
Best P. N., Longair M. S., Röttgering H. J. A., 1998, MNRAS, 295, 549
Best P. N., Röttgering H. J. A., Lehnert M. D., 1999, MNRAS, 310, 223
Best P. N., Röttgering H. J. A., Lehnert M. D., 2000, MNRAS, 315, 21
Blake C., Wall J., 2002, MNRAS, 329, L37
Bremer M. N., Rengelink R., Saunders R., Röttgering H. J. A., Miley G. K., Snellen I. A. G., 1999, in Bremer M. N., Jackson N., Pérez–Fournon I., eds, Observational Cosmology with the New Radio Surveys. Kluwer Academic Publishers
Chambers K. C., Miley G. K., van Breugel W. J. M., 1987, Nat, 329, 604
Condon J. J., 1997, PASP, 109, 166
Condon J. J., Cotton W. D., Greisen E. W., Yin Q. F., Perley R. A., Taylor G. B., Broderick J. J., 1998, AJ, 115, 1693
Daddi E., Röttgering H. J. A., Labbé I., Rudnick G., Franx M., Moorwood A. F. M., Rix H. W., van der Werf P. P., van Dokkum P. G., 2003, ApJ, 558, 50

de Ruiter H. R., Arp H. C., Willis A. G., 1977, A&A Supp., 28, 211

Dunlop J. S., Peacock J., 1990, MNRAS, 247, 19

Dunlop J. S., Peacock J. A., Savage A., Lilly S. J., Heasley J. N., Simon A. J. B., 1989, MNRAS, 238, 1171

Eales S. A., 1985a, MNRAS, 217, 167

Eales S. A., 1985b, MNRAS, 217, 149

Eales S. A., 1985c, MNRAS, 213, 899

Eales S. A., Rawlings S., 1996, ApJ, 460, 68

Fanaroff B. L., Riley J. M., 1974, MNRAS, 167, 31P

Finn R. A., Impey C. D., Hooper E. J., 2001, ApJ, 557, 578

Gavazzi G., Boselli A., 1999, A&A, 343, 86

Greisen E. W., Calabretta M. R., 2002, A&A, 395, 1061

Inskip K. J., Best P. N., Longair M. S., MacKay D. J. C., 2002, MNRAS, 329, 277

Inskip K. J., Best P. N., Longair M. S., Rawlings S., Röttgering H. J. A., Eales S., 2003, MNRAS, submitted

Jarvis M. J., Rawlings S., Willott C. J., Blundell K. M., Eales S., Lacy M., 2001, MNRAS, 327, 907

Kormendy J., Gebhardt K., 2001, p. 363

Lacy M., Hill G., Kaiser M. E., Rawlings S., 1993, MNRAS, 263, 707

Laing R. A., Riley J. M., Longair M. S., 1983, MNRAS, 204, 151

Lara L., Cotton W. D., Feretti L., Giovannini G., Marcaide J. M., Marquez I., Venturi T., 2001, A&A, 370, 409

Lilly S. J., Longair M. S., 1984, MNRAS, 211, 833

Machalski J., Godlowski W., 2000, A&A, 360, 463

McCarthy P. J., Kapahi V. K., van Breugel W., Persson S. E., Athreya R. M., Subrahmanya C. R., 1996, ApJ Supp., 107, 19

McCarthy P. J., van Breugel W. J. M., Kapahi V. K., 1991, ApJ, 371, 478

McCarthy P. J., van Breugel W. J. M., Spinrad H., Djorgovski S., 1987, ApJ, 321, L29

Mobasher B., Cram L., Georgakakis A., Hopkins A., 1999, MNRAS, 308, 45

Neeser M. J., Eales S. A., Law–Green J. D., Leahy J. P., Rawlings S., 1995, ApJ, 451, 76

Nonino M., Bertin E., da Costa L., Deul E., Erben T., Olsen L., Prandoni I., Scodeggio M., Wicenec A., Wichmann R., Benoist C., Freudling W., Guarnieri M. D., Hook I., Hook R., Mendez R., Savaglio S., Silva D., Slijkhuis R., 1999, A&A Supp., 137, 51

Oort M. J. A., Katgert P., Windhorst R. A., 1987, Nat, 328, 500

Overzier R. A., Röttgering H. J. A., Rengelink R. B., Wilman R., 2003, A&A, in press, astro-ph/0304160

Peacock J. A., 1985, MNRAS, 217, 601

Poggianti B. M., 1997, A&A Supp., 122, 399

Pooley D. M., Waldrum E. M., Riley J. M., 1998, MNRAS, 298, 637

Porciani C., Giavalisco M., 2002, ApJ, 565, 24

Prestage R. M., Peacock J. A., 1988, MNRAS, 230, 131

Rawlings S., Eales S. A., Lacy M., 2001, MNRAS, 322, 523

Rengelink R. B., 1998, Ph.D. thesis, Sterrewacht, University of Leiden

Richards E. A., Kellermann K. I., Formalont E. B., Windhorst R. A., Partridge R. B., 1998, AJ, 116, 1039

Richstone D., 1998, Nat, 395, 138

Richter G. A., 1975, Astronomische Nachrichten, 295, 65

Sadler E. M. et al. 2002, MNRAS, 329, 227

Snellen I. A. G., Best P. N., 2001, MNRAS, 328, 897

Snellen I. A. G., Bremer M. N., Schilizzi R. T., Miley G. K., van Ojik R., 1996, MNRAS, 279, 1294

Soneira R. M., Peebles P. J. E., 1977, ApJ, 211, 1

Soneira R. M., Peebles P. J. E., 1978, AJ, 83, 845

Spinrad H., Djorgovski S., Marr J., Aguilar L. A., 1985, PASP, 97, 932

Waddington I., Dunlop J. S., Peacock J. A., Windhorst R. A., 2001, MNRAS, 328, 882

Wall J. V., Jackson C. A., 1997, MNRAS, 290, L22

Wall J. V., Peacock J. A., 1985, MNRAS, 216, 173

Willott C. J., Rawlings S., Blundell K. M., Lacy M., 1998, MNRAS, 300, 625

Willott C. J., Rawlings S., Blundell K. M., Lacy M., Eales S. A., 2001, MNRAS, 322, 536

Willott C. J., Rawlings S., Blundell K. M., Lacy M., Hill G., Scott S. E., 2002, MNRAS, 335, 1120

Willott C. J., Rawlings S., Jarvis M. J., Blundell K. M., 2003, MNRAS, in press; astro-ph/0209439

Wold M., Lacy M., Lilje P. B., Serjeant S., 2000, MNRAS, 316, 267

Woo J.-H., Urry C. M., 2002, ApJ, 581, L5

APPENDIX A: PROPERTIES OF THE RADIO SOURCES

In this appendix, properties of the radio sources are provided. Table A1 provides details of the original EIS–NVSS sample of radio sources, and the observations of these. Radio maps of those sources which are located within the region of optical imaging of the EIS survey are shown in Figure A1, overlaid upon greyscale images taken from the *I*–band EIS data. Radio maps of those which lie outside of the EIS Patch D are shown in Figure A2. Table A2 provides the properties of the radio source components, as derived from these new radio maps.

Table A1. Details of the EIS-NVSS sample of radio sources. The flux densities quoted are at 1.4 GHz as extracted from the most recent version of the NVSS catalogue (version 2.17, issued July 2002). The rms noise is that on the final image produced from the new VLA observations (after combination of array configurations where appropriate) presented in this paper.

Source	IAU Name	RA (NVSS) Dec (J2000)		$S^{\mathrm{NVSS}}_{1.4\,\mathrm{GHz}}$ [mJy]	Observation Date BnA array	CnB array	rms [μJy]
EISD1	NVSS-J095129-2050	09 51 29.17	-20 50 28.6	659.5 ± 19.8	15/06/1998	—	65
EISD2	NVSS-J094650-2020	09 46 50.28	-20 20 44.1	452.3 ± 13.6	15/06/1998	—	58
EISD3	NVSS-J095031-2102	09 50 31.40	-21 02 43.0	355.3 ± 10.7	15/06/1998	—	49
EISD4	NVSS-J094905-1957	09 49 05.67	-19 57 10.6	302.1 ± 10.0	15/06/1998	—	35
EISD5	NVSS-J095953-2148	09 59 53.89	-21 48 47.7	299.6 ± 10.5	15/06/1998	—	47
EISD6	NVSS-J094953-2156	09 49 53.57	-21 56 17.4	283.0 ± 9.5	15/06/1998	—	33
EISD7	NVSS-J095143-2123	09 51 43.69	-21 23 56.4	246.2 ± 7.4	15/06/1998	30/04/2001	32
EISD8	NVSS-J095344-2135	09 53 44.01	-21 35 51.7	244.7 ± 8.2	15/06/1998	—	34
EISD9	NVSS-J095812-2144	09 58 12.96	-21 44 41.0	196.9 ± 5.9	15/06/1998	—	48
EISD10	NVSS-J094557-2116	09 45 57.05	-21 16 48.2	148.2 ± 5.1	15/06/1998	—	42
EISD11	NVSS-J095730-2130	09 57 30.00	-21 30 58.2	126.3 ± 3.8	15/06/1998	—	44
EISD12	NVSS-J094935-2156	09 49 35.38	-21 56 23.2	118.2 ± 3.6	15/06/1998	—	40
EISD13	NVSS-J094427-2116	09 44 27.26	-21 16 10.8	100.8 ± 3.1	15/06/1998	—	48
EISD14	NVSS-J095951-2053	09 59 51.08	-20 53 18.9	87.2 ± 2.7	15/06/1998	—	38
EISD15	NVSS-J095329-2002	09 53 29.54	-20 02 13.0	78.1 ± 2.4	15/06/1998	—	40
EISD16	NVSS-J094727-2126	09 47 27.03	-21 26 21.0	79.4 ± 2.9	15/06/1998	30/04/2001	28
EISD17	NVSS-J094433-2105	09 44 33.17	-21 05 07.2	73.9 ± 2.3	15/06/1998	—	45
EISD18	NVSS-J094641-2029	09 46 41.16	-20 29 26.0	70.4 ± 2.6	15/06/1998	—	47
EISD19	NVSS-J094508-2038	09 45 08.44	-20 38 07.9	69.1 ± 2.1	15/06/1998	—	42
EISD20	NVSS-J095428-2156	09 54 28.91	-21 56 53.6	66.3 ± 2.7	15/06/1998	—	29
EISD21	NVSS-J095447-2059	09 54 47.70	-20 59 43.4	65.6 ± 2.4	15/06/1998	—	43
EISD22	NVSS-J094651-2053	09 46 51.17	-20 53 17.5	63.0 ± 1.9	15/06/1998	—	35
EISD23	NVSS-J095751-2133	09 57 51.31	-21 33 21.5	61.7 ± 2.3	15/06/1998	—	60
EISD24	NVSS-J095242-1958	09 52 42.99	-19 58 20.0	61.5 ± 2.3	15/06/1998	—	32
EISD25	NVSS-J095513-2123	09 55 13.61	-21 23 03.2	58.3 ± 1.8	15/06/1998	—	32
EISD26	NVSS-J095904-2008	09 59 04.87	-20 08 05.0	57.7 ± 2.2	15/06/1998	—	37
EISD27	NVSS-J095330-2135	09 53 30.49	-21 35 58.9	55.1 ± 2.1	15/06/1998	—	46
EISD28	NVSS-J094758-2121	09 47 58.99	-21 21 50.6	54.0 ± 1.7	15/06/1998	—	41
EISD29	NVSS-J095730-2132	09 57 30.82	-21 32 37.7	52.9 ± 1.7	15/06/1998	—	32
EISD30	NVSS-J094604-2115	09 46 04.78	-21 15 08.8	54.2 ± 2.1	15/06/1998	—	36
EISD31	NVSS-J095629-2001	09 56 29.93	-20 01 30.5	52.4 ± 2.0	15/06/1998	—	32
EISD32	NVSS-J095438-2104	09 54 38.38	-21 04 25.3	51.0 ± 1.6	15/06/1998	—	46
EISD33	NVSS-J095433-2205	09 54 33.72	-22 05 22.2	50.1 ± 1.9	15/06/1998	—	40
EISD34	NVSS-J094804-2147	09 48 04.06	-21 47 36.5	49.2 ± 1.9	15/06/1998	—	33
EISD35	NVSS-J095902-2039	09 59 02.43	-20 39 45.7	47.0 ± 2.1	15/06/1998	—	42
EISD36	NVSS-J095217-2008	09 52 17.76	-20 08 35.3	44.4 ± 1.4	15/06/1998	—	29
EISD37	NVSS-J095825-2044	09 58 25.97	-20 44 51.3	42.5 ± 1.4	15/06/1998	—	31
EISD38	NVSS-J094631-2026	09 46 31.42	-20 26 10.2	40.1 ± 1.9	15/06/1998	—	46
EISD39	NVSS-J094815-2140	09 48 15.71	-21 40 05.1	38.2 ± 1.6	15/06/1998	—	36
EISD40	NVSS-J094556-2028	09 45 56.53	-20 28 31.3	37.8 ± 2.0	15/06/1998	30/04/2001	35
EISD41	NVSS-J094519-2142	09 45 19.62	-21 42 39.5	37.3 ± 1.5	15/06/1998	—	45
EISD42	NVSS-J095827-2105	09 58 27.40	-21 05 26.5	36.0 ± 1.2	15/06/1998	—	35
EISD43	NVSS-J095141-2011	09 51 41.06	-20 11 17.9	35.3 ± 1.5	15/06/1998	—	25
EISD44	NVSS-J095150-2125	09 51 50.39	-21 25 14.4	33.9 ± 2.3	15/06/1998	30/04/2001	22
EISD45	NVSS-J095304-2044	09 53 04.75	-20 44 09.6	34.3 ± 1.1	15/06/1998	—	33
EISD46	NVSS-J094455-2017	09 44 55.53	-20 17 14.6	34.3 ± 1.4	15/06/1998	—	45
EISD47	NVSS-J094753-2147	09 47 53.64	-21 47 19.2	34.2 ± 1.1	15/06/1998	—	34
EISD48	NVSS-J095452-2119	09 54 52.43	-21 19 28.8	34.1 ± 1.4	15/06/1998	—	34
EISD49	NVSS-J095925-2006	09 59 25.82	-20 06 40.3	32.9 ± 2.0	15/06/1998	—	39
EISD50	NVSS-J095724-2203	09 57 24.19	-22 03 52.6	33.1 ± 1.1	15/06/1998	—	44
EISD51	NVSS-J094933-2127	09 49 33.26	-21 27 07.7	32.3 ± 1.1	15/06/1998	—	29
EISD52	NVSS-J094919-2151	09 49 19.33	-21 51 35.4	31.8 ± 1.4	15/06/1998	—	35
EISD53	NVSS-J095116-2056	09 51 16.85	-20 56 35.2	31.7 ± 1.1	15/06/1998	—	50
EISD54	NVSS-J094836-2106	09 48 36.08	-21 06 23.0	31.5 ± 1.1	15/06/1998	—	32
EISD55	NVSS-J095058-2114	09 50 58.79	-21 14 18.8	30.9 ± 1.3	15/06/1998	—	35
EISD56	NVSS-J094728-2128	09 47 28.89	-21 28 35.8	28.5 ± 2.9	15/06/1998	30/04/2001	28
EISD57	NVSS-J095816-2018	09 58 16.61	-20 18 54.3	29.6 ± 1.3	15/06/1998	—	42
EISD58	NVSS-J094918-2054	09 49 18.12	-20 54 52.5	27.5 ± 1.7	15/06/1998	—	45
EISD59	NVSS-J094453-2046	09 44 53.65	-20 46 35.9	28.6 ± 1.0	15/06/1998	—	39
EISD60	NVSS-J095201-2115	09 52 01.84	-21 15 50.7	26.5 ± 0.9	15/06/1998	—	29
EISD61	NVSS-J095940-2034	09 59 40.85	-20 34 48.3	26.3 ± 1.2	15/06/1998	—	40

Table A1. *continued.* Details of the EIS–NVSS sample of radio sources.

Source	IAU Name	RA (NVSS) Dec (J2000)		$S_{1.4\,\mathrm{GHz}}^{\mathrm{NVSS}}$ [mJy]	Observation Date BnA array	CnB array	rms [μJy]
EISD62	NVSS-J095427-2029	09 54 27.08	-20 29 46.7	26.1 ± 0.9	15/06/1998	—	28
EISD63	NVSS-J094703-2050	09 47 03.48	-20 50 02.0	25.2 ± 0.9	15/06/1998	—	33
EISD64	NVSS-J095259-2148	09 52 59.24	-21 48 41.4	26.4 ± 0.9	15/06/1998	—	34
EISD65	NVSS-J095403-2025	09 54 03.09	-20 25 13.3	25.2 ± 0.9	15/06/1998	—	31
EISD66	NVSS-J095743-2006	09 57 43.07	-20 06 36.1	25.5 ± 1.2	15/06/1998	—	46
EISD67	NVSS-J095323-2013	09 53 23.15	-20 13 43.6	23.8 ± 0.9	15/06/1998	—	26
EISD68	NVSS-J095428-2039	09 54 28.16	-20 39 28.2	24.2 ± 0.9	15/06/1998	—	46
EISD69	NVSS-J095212-2102	09 52 12.79	-21 02 36.2	22.3 ± 0.8	15/06/1998	—	36
EISD70	NVSS-J095130-2204	09 51 30.71	-22 04 27.7	22.3 ± 1.1	15/06/1998	—	30
EISD71	NVSS-J094930-2023	09 49 30.68	-20 23 33.4	21.4 ± 0.8	15/06/1998	—	27
EISD72	NVSS-J094542-2115	09 45 42.59	-21 15 42.3	21.7 ± 0.8	15/06/1998	—	41
EISD73	NVSS-J095546-2126	09 55 46.10	-21 26 55.6	18.9 ± 3.3	15/06/1998	30/04/2001	20
EISD74	NVSS-J095320-2143	09 53 20.62	-21 43 58.7	21.4 ± 0.8	15/06/1998	—	53
EISD75	NVSS-J095122-2151	09 51 22.83	-21 51 52.0	21.7 ± 0.8	15/06/1998	—	32
EISD76	NVSS-J095132-2100	09 51 32.53	-21 00 27.2	21.6 ± 1.1	15/06/1998	—	36
EISD77	NVSS-J095523-2128	09 55 23.78	-21 28 30.5	19.6 ± 2.3	15/06/1998	30/04/2001	18
EISD78	NVSS-J095043-2126	09 50 43.23	-21 26 37.6	20.8 ± 1.1	15/06/1998	—	34
EISD79	NVSS-J094855-2103	09 48 55.29	-21 03 57.4	20.7 ± 0.8	15/06/1998	—	29
EISD80	NVSS-J095121-2129	09 51 21.17	-21 29 54.6	20.7 ± 1.1	15/06/1998	—	36
EISD81	NVSS-J094842-2152	09 48 42.34	-21 52 26.1	19.1 ± 1.1	15/06/1998	—	34
EISD82	NVSS-J094801-2009	09 48 01.89	-20 09 11.7	18.5 ± 0.7	15/06/1998	—	37
EISD83	NVSS-J095148-2031	09 51 48.71	-20 31 53.4	18.9 ± 0.7	15/06/1998	—	28
EISD84	NVSS-J094945-2150	09 49 45.77	-21 50 04.8	18.4 ± 0.7	15/06/1998	—	35
EISD85	NVSS-J094859-2050	09 48 59.96	-20 50 07.9	18.1 ± 1.0	15/06/1998	09/06/2002	27
EISD86	NVSS-J095512-2123	09 55 12.44	-21 23 09.6	15.3 ± 3.3	15/06/1998	—	33
EISD87	NVSS-J095726-2013	09 57 26.12	-20 13 04.3	17.9 ± 1.0	15/06/1998	—	28
EISD88	NVSS-J094529-2118	09 45 29.43	-21 18 48.8	18.3 ± 0.7	15/06/1998	—	49
EISD89	NVSS-J095731-2120	09 57 31.82	-21 20 25.4	17.3 ± 0.7	15/06/1998	—	52
EISD90	NVSS-J095046-2132	09 50 46.78	-21 32 51.1	17.4 ± 1.1	15/06/1998	—	29
EISD91	NVSS-J095451-2130	09 54 51.94	-21 30 17.5	17.2 ± 0.7	15/06/1998	—	28
EISD92	NVSS-J095602-2156	09 56 02.35	-21 56 02.9	17.0 ± 0.7	15/06/1998	—	29
EISD93	NVSS-J095541-2039	09 55 41.86	-20 39 39.3	16.7 ± 0.7	15/06/1998	—	37
EISD94	NVSS-J095628-2048	09 56 28.15	-20 48 44.5	16.2 ± 0.7	15/06/1998	—	40
EISD95	NVSS-J094428-2038	09 44 28.80	-20 38 00.3	16.2 ± 1.0	15/06/1998	—	43
EISD96	NVSS-J094929-2129	09 49 29.71	-21 29 38.8	16.0 ± 0.7	15/06/1998	—	28
EISD97	NVSS-J094925-2037	09 49 25.95	-20 37 24.5	16.5 ± 0.7	15/06/1998	—	30
EISD98	NVSS-J094526-2033	09 45 26.88	-20 33 52.8	15.7 ± 1.0	15/06/1998	—	43
EISD99	NVSS-J094446-2050	09 44 46.39	-20 50 00.8	15.7 ± 1.1	15/06/1998	—	45
EISD100	NVSS-J095843-2051	09 58 43.82	-20 51 30.1	15.4 ± 0.7	15/06/1998	—	35
EISD101	NVSS-J095844-2031	09 58 44.74	-20 31 15.0	14.8 ± 0.7	15/06/1998	—	27
EISD102	NVSS-J095746-2123	09 57 46.01	-21 23 26.5	15.3 ± 0.7	15/06/1998	—	37
EISD103	NVSS-J095545-2125	09 55 45.86	-21 25 27.0	13.5 ± 1.2	15/06/1998	30/04/2001	20
EISD104	NVSS-J094942-2037	09 49 42.89	-20 37 44.5	15.0 ± 0.7	15/06/1998	—	31
EISD105	NVSS-J095416-2129	09 54 16.90	-21 29 12.4	14.5 ± 1.4	19/06/1998	30/04/2001	40
EISD106	NVSS-J094548-2159	09 45 48.34	-21 59 08.6	14.6 ± 1.1	15/06/1998	—	43
EISD107	NVSS-J095559-2042	09 55 59.27	-20 42 53.2	14.6 ± 0.7	15/06/1998	—	26
EISD108	NVSS-J095741-1955	09 57 41.91	-19 55 57.0	14.2 ± 1.0	15/06/1998	—	25
EISD109	NVSS-J094447-2058	09 44 47.38	-20 58 14.7	14.0 ± 0.6	15/06/1998	—	42
EISD110	NVSS-J095453-2115	09 54 53.16	-21 15 12.3	14.5 ± 0.6	15/06/1998	—	32
EISD111	NVSS-J094556-2120	09 45 56.28	-21 20 48.9	13.2 ± 0.6	15/06/1998	30/04/2001	15
EISD112	NVSS-J095523-2130	09 55 23.96	-21 30 02.9	13.4 ± 1.0	15/06/1998	30/04/2001	18
EISD113	NVSS-J095053-2133	09 50 53.40	-21 33 01.4	13.6 ± 0.6	15/06/1998	—	37
EISD114	NVSS-J094734-2126	09 47 34.67	-21 26 58.5	12.8 ± 0.6	15/06/1998	30/04/2001	28
EISD115	NVSS-J094445-2146	09 44 45.29	-21 46 21.0	13.4 ± 0.6	15/06/1998	—	36
EISD116	NVSS-J095129-2016	09 51 29.60	-20 16 41.5	13.5 ± 0.6	15/06/1998	—	28
EISD117	NVSS-J095309-2001	09 53 09.44	-20 01 22.3	13.0 ± 1.0	15/06/1998	—	37
EISD118	NVSS-J095724-2129	09 57 24.26	-21 29 43.3	10.6 ± 1.9	15/06/1998	—	35
EISD119	NVSS-J094520-2201	09 45 20.94	-22 01 18.1	13.1 ± 0.6	15/06/1998	—	43
EISD120	NVSS-J094804-2034	09 48 04.23	-20 34 35.9	13.2 ± 0.6	15/06/1998	—	33
EISD121	NVSS-J095456-2205	09 54 56.93	-22 05 05.8	10.8 ± 1.6	15/06/1998	—	27
EISD122	NVSS-J095255-2052	09 52 55.86	-20 52 07.0	12.6 ± 1.1	15/06/1998	30/04/2001	18
EISD123	NVSS-J095421-2148	09 54 21.85	-21 48 04.1	12.2 ± 1.2	15/06/1998	—	37
EISD124	NVSS-J094810-2001	09 48 10.05	-20 01 58.1	12.1 ± 1.4	15/06/1998	30/04/2001	18

Table A1. *continued.* Details of the EIS–NVSS sample of radio sources.

Source	IAU Name	RA (NVSS) Dec (J2000)		$S^{\mathrm{NVSS}}_{1.4\,\mathrm{GHz}}$ [mJy]	Observation Date BnA array	CnB array	rms [μJy]
EISD125	NVSS-J094521-2043	09 45 21.17	-20 43 18.3	12.2 ± 0.6	15/06/1998	—	42
EISD126	NVSS-J095436-2144	09 54 36.25	-21 44 37.9	12.0 ± 1.2	15/06/1998	—	42
EISD127	NVSS-J094822-2105	09 48 22.17	-21 05 08.4	12.7 ± 0.6	15/06/1998	—	36
EISD128	NVSS-J095816-2058	09 58 16.47	-20 58 23.7	10.5 ± 1.3	15/06/1998	—	32
EISD129	NVSS-J095620-2203	09 56 20.42	-22 03 47.7	11.3 ± 0.6	15/06/1998	—	40
EISD130	NVSS-J094935-2158	09 49 35.26	-21 58 08.4	11.8 ± 0.6	15/06/1998	—	42
EISD131	NVSS-J094925-2005	09 49 25.83	-20 05 18.4	12.0 ± 0.6	15/06/1998	—	36
EISD132	NVSS-J094618-2037	09 46 18.92	-20 37 58.4	12.2 ± 0.6	15/06/1998	—	44
EISD133	NVSS-J095702-2156	09 57 02.06	-21 56 50.7	11.6 ± 0.6	15/06/1998	—	33
EISD134	NVSS-J094649-2116	09 46 49.75	-21 16 47.0	11.1 ± 1.1	15/06/1998	30/04/2001	13
EISD135	NVSS-J095851-2110	09 58 51.31	-21 10 20.4	11.4 ± 1.1	15/06/1998	—	38
EISD136	NVSS-J095048-2154	09 50 48.49	-21 54 55.0	11.5 ± 0.6	15/06/1998	—	40
EISD137	NVSS-J094813-1959	09 48 13.10	-19 59 54.7	10.0 ± 1.2	15/06/1998	30/04/2001	18
EISD138	NVSS-J094724-2105	09 47 24.55	-21 05 05.6	10.6 ± 0.6	15/06/1998	—	39
EISD139	NVSS-J095250-2131	09 52 50.33	-21 31 47.3	11.4 ± 0.6	15/06/1998	—	39
EISD140	NVSS-J095933-2114	09 59 33.68	-21 14 50.8	8.9 ± 1.6	15/06/1998	—	40
EISD141	NVSS-J095511-2030	09 55 11.87	-20 30 20.6	10.1 ± 1.3	15/06/1998	30/04/2001	25
EISD142	NVSS-J095607-2005	09 56 07.01	-20 05 40.6	10.5 ± 0.6	15/06/1998	—	36
EISD143	NVSS-J095735-2029	09 57 35.04	-20 29 31.7	9.6 ± 0.6	15/06/1998	—	36
EISD144	NVSS-J094450-2017	09 44 50.70	-20 17 35.2	10.5 ± 0.6	15/06/1998	—	60
EISD145	NVSS-J095739-2003	09 57 39.46	-20 03 18.5	10.7 ± 0.6	15/06/1998	—	28
EISD146	NVSS-J095642-2119	09 56 42.22	-21 19 41.8	9.8 ± 0.6	15/06/1998	—	39
EISD147	NVSS-J095857-2034	09 58 57.31	-20 34 19.2	8.1 ± 1.3	15/06/1998	—	38
EISD148	NVSS-J094538-2111	09 45 38.34	-21 11 12.1	10.3 ± 1.0	15/06/1998	09/06/2002	30
EISD149	NVSS-J094744-2112	09 47 44.72	-21 12 29.8	10.0 ± 0.6	15/06/1998	—	48
EISD150	NVSS-J094710-2035	09 47 10.23	-20 35 53.0	9.7 ± 0.6	15/06/1998	—	53
EISD151	NVSS-J095553-2127	09 55 53.71	-21 27 12.1	4.5 ± 0.8	15/06/1998	30/04/2001	20
EISD152	NVSS-J095927-2003	09 59 27.65	-20 03 14.8	9.7 ± 0.6	15/06/1998	—	43
EISD153	NVSS-J095649-2035	09 56 49.68	-20 35 23.9	10.2 ± 0.6	15/06/1998	—	36
EISD154	NVSS-J095210-2050	09 52 10.86	-20 50 08.2	10.1 ± 0.6	15/06/1998	—	52
EISD155	NVSS-J095724-2022	09 57 24.53	-20 22 36.3	9.6 ± 1.0	15/06/1998	—	37
EISD156	NVSS-J095637-2019	09 56 37.01	-20 19 02.6	9.0 ± 0.6	15/06/1998	—	37
EISD157	NVSS-J094902-2115	09 49 02.13	-21 15 04.7	9.4 ± 0.6	15/06/1998	—	42
EISD158	NVSS-J094443-2144	09 44 43.88	-21 44 38.5	9.3 ± 0.6	15/06/1998	—	60
EISD159	NVSS-J095357-2036	09 53 57.45	-20 36 52.0	9.1 ± 0.6	15/06/1998	—	34
EISD160	NVSS-J095849-2117	09 58 49.60	-21 17 35.5	8.8 ± 0.6	19/06/1998	—	29
EISD161	NVSS-J094748-2048	09 47 48.46	-20 48 35.7	9.4 ± 0.6	15/06/1998	—	39
EISD162	NVSS-J095638-2010	09 56 38.86	-20 10 44.1	4.1 ± 0.8	19/06/1998	09/06/2002	30
EISD163	NVSS-J094910-2021	09 49 10.67	-20 21 52.5	8.7 ± 0.6	19/06/1998	—	33
EISD164	NVSS-J095201-2024	09 52 01.26	-20 24 54.0	9.0 ± 0.5	19/06/1998	—	39
EISD165	NVSS-J095410-2158	09 54 10.47	-21 58 00.6	9.5 ± 0.6	19/06/1998	—	45
EISD166	NVSS-J095604-2144	09 56 04.41	-21 44 36.3	9.6 ± 0.6	19/06/1998	—	41
EISD167	NVSS-J094602-2151	09 46 02.57	-21 51 40.4	7.9 ± 0.6	19/06/1998	—	20
EISD168	NVSS-J094450-2007	09 44 50.35	-20 07 35.5	8.4 ± 0.6	19/06/1998	—	48
EISD169	NVSS-J095148-2133	09 51 48.92	-21 33 37.2	8.2 ± 0.6	19/06/1998	—	58
EISD170	NVSS-J095226-2001	09 52 26.52	-20 01 05.2	8.3 ± 0.6	19/06/1998	—	46
EISD171	NVSS-J094750-2142	09 47 50.04	-21 42 17.2	8.4 ± 1.3	19/06/1998	—	43
EISD172	NVSS-J095722-2101	09 57 22.22	-21 01 03.4	8.2 ± 0.5	19/06/1998	—	35
EISD173	NVSS-J095431-2035	09 54 31.12	-20 35 40.0	8.7 ± 0.5	19/06/1998	—	40
EISD174	NVSS-J094902-2016	09 49 02.62	-20 16 09.8	8.3 ± 0.5	19/06/1998	—	46
EISD175	NVSS-J094922-2118	09 49 22.34	-21 18 19.5	8.4 ± 0.5	19/06/1998	—	45
EISD176	NVSS-J095820-2139	09 58 20.40	-21 39 13.3	7.5 ± 1.2	19/06/1998	—	58
EISD177	NVSS-J095527-2046	09 55 27.05	-20 46 07.9	7.1 ± 0.6	19/06/1998	—	43
EISD178	NVSS-J094748-2100	09 47 48.27	-21 00 44.9	7.8 ± 0.6	19/06/1998	—	37
EISD179	NVSS-J094959-2127	09 49 59.68	-21 27 19.0	6.0 ± 0.6	19/06/1998	—	48
EISD180	NVSS-J094912-2200	09 49 12.22	-22 00 29.2	6.9 ± 0.6	19/06/1998	—	53
EISD181	NVSS-J095441-2049	09 54 41.98	-20 49 47.1	7.5 ± 0.6	19/06/1998	—	33
EISD182	NVSS-J094949-2134	09 49 49.04	-21 34 32.8	7.8 ± 0.6	19/06/1998	—	40
EISD183	NVSS-J095129-2025	09 51 29.20	-20 25 40.9	7.8 ± 1.2	19/06/1998	30/04/2001	14
EISD184	NVSS-J094507-2109	09 45 07.57	-21 09 28.0	6.4 ± 0.6	19/06/1998	—	52
EISD185	NVSS-J095212-2140	09 52 12.69	-21 40 27.6	4.0 ± 0.7	19/06/1998	30/04/2001	18
EISD186	NVSS-J094924-2111	09 49 24.70	-21 11 10.0	8.3 ± 0.5	19/06/1998	—	52
EISD187	NVSS-J095038-2141	09 50 38.48	-21 41 15.1	7.4 ± 1.2	19/06/1998	30/04/2001	23

Table A1. *continued.* Details of the EIS–NVSS sample of radio sources.

Source	IAU Name	RA (NVSS) Dec (J2000)		$S^{\mathrm{NVSS}}_{1.4\,\mathrm{GHz}}$ [mJy]	Observation Date		rms [μJy]
					BnA array	CnB array	
EISD188	NVSS-J094746-2127	09 47 46.11	-21 27 44.3	6.1 ± 0.6	19/06/1998	—	47
EISD189	NVSS-J094552-2014	09 45 52.01	-20 14 41.8	6.6 ± 0.6	19/06/1998	—	60
EISD190	NVSS-J095937-2038	09 59 37.53	-20 38 21.9	7.4 ± 0.5	19/06/1998	—	44
EISD191	NVSS-J095027-2148	09 50 27.69	-21 48 09.2	5.4 ± 0.6	19/06/1998	—	41
EISD192	NVSS-J095912-2012	09 59 12.27	-20 12 54.4	5.4 ± 0.6	19/06/1998	—	49
EISD193	NVSS-J095056-1955	09 50 56.59	-19 55 08.3	5.9 ± 0.6	19/06/1998	—	36
EISD194	NVSS-J094527-2057	09 45 27.50	-20 57 47.8	3.8 ± 0.7	19/06/1998	30/04/2001	17
EISD195	NVSS-J095715-2030	09 57 15.62	-20 30 34.0	6.3 ± 0.6	19/06/1998	—	42
EISD196	NVSS-J095002-2205	09 50 02.94	-22 05 34.9	5.1 ± 0.6	19/06/1998	—	57
EISD197	NVSS-J094522-2036	09 45 22.09	-20 36 12.9	4.2 ± 0.7	19/06/1998	—	57
EISD198	NVSS-J095850-2108	09 58 50.83	-21 08 14.9	6.1 ± 0.6	19/06/1998	—	43
EISD199	NVSS-J094526-2154	09 45 26.51	-21 54 57.3	6.8 ± 0.5	19/06/1998	—	43

Figure A1. *See attached jpeg files.* Radio maps (in contours) of those radio sources within the EIS Patch D, with greyscale representations of the EIS *I*–band image overlaid. The radio contour levels are at $(-1,1,2,4,8,16,32,64,128,256,512,1024) \times 3\sigma$, where σ is the rms noise on the radio map, given in Table A1; any negative contour is shown as a dashed line. The label above each figure indicates which source is being shown. All figures are shown with an equivalent grey-scale level, except for EISD162 where this is changed in order to allow the radio source host galaxy to be distinguished from the nearby bright star, and the EISD123, EISD163 and EISD191 where the contrast is lowered to show details of the host galaxy. Likely optical host galaxies are labelled with crosshairs.

Figure A2. *See attached jpeg files.* Radio maps (in contours) of those radio sources outside the EIS Patch D. The radio contour levels are at $(-1,1,2,4,8,16,32,64,128,256,512,1024) \times 3\sigma$, where σ is the rms noise on the radio map, given in Table A1; any negative contour is shown as a dashed line. The label above each figure indicates which source is being shown.

Figure A3. *See attached jpeg files.* Radio maps (in contours) of the three additional radio sources to be added to the CENSORS sample (CENSORS-X1,X2 and X3), with greyscale representations of the EIS *I*–band images overlaid. Also, the NVSS map of the potential large double to be included in the sample (known as CENSORS-D1). The radio contour levels are at $(-1,1,2,4,8,16,32,64,128,256,512,1024) \times [100\mu\mathrm{Jy},130\mu\mathrm{Jy},135\mu\mathrm{Jy}, 1\mathrm{mJy}]$ for CENSORS-X1,X2,X3 and D1 respectively. Note that all of the CENSOR-X1-3 sources show unphysical elongations due to bandwidth smearing, since they are observed considerably off–axis in the radio observations (but they have been corrected for primary beam attenuation effects).

APPENDIX B: THE OPTICAL COUNTERPARTS

In this appendix, the technique used to identify optical galaxies in the EIS catalogue as the host galaxies of the radio sources is described. Then, Table B1 provides details of the optical counterparts, as determined from the EIS database.

B1   Maximum likelihood analysis

The likelihood ratio technique (e.g. Richter 1975, de Ruiter et al. 1977) can be used to statistically investigate whether a proposed optical identification is the real counterpart of a radio source. In this method, the dimensionless difference between the radio and optical positions is defined as:

$$r = \left(\frac{\Delta\alpha^2}{\sigma_\alpha^2} + \frac{\Delta\delta^2}{\sigma_\delta^2} \right)^{\frac{1}{2}},$$

where $\Delta\alpha$ and $\Delta\delta$ are the differences in right ascension and declination between the radio and optical positions, and σ_α and σ_δ are the positional standard errors on these differences. These have contributions from the uncertainties in both the radio and optical positions: $\sigma_\alpha^2 = \sigma_{\alpha_{\rm rad}}^2 + \sigma_{\alpha_{\rm opt}}^2$, and $\sigma_\delta^2 = \sigma_{\delta_{\rm rad}}^2 + \sigma_{\delta_{\rm opt}}^2$. The radio uncertainties for a typical unresolved component are about ± 0.3 arcsec in each direction. Defining the astrometry of the radio frames to be absolute, the uncertainties in the optical positions are dominated by the radio–optical astrometric errors, which are of order ± 0.2 arcsec.

Assuming a random distribution of objects in the EIS survey, the probability of the nearest random object (c) lying at a radius of between r and $r + {\rm d}r$ is governed by a Poisson process and can be written as ${\rm d}p(r|{\rm c}) = 2\lambda r e^{-\lambda r^2} {\rm d}r$, where $\lambda = \pi \sigma_\alpha \sigma_\delta \rho$ and ρ is the number of objects per square arcsecond in the EIS catalogue. The probability of finding the true optical counterpart (id) of the radio source at a distance between r and $r + {\rm d}r$ can be represented by a Rayleigh distribution: ${\rm d}p(r|{\rm id}) = r e^{-\lambda r^2/2} {\rm d}r$. The likelihood ratio, defined as:

$$LR(r) \equiv \frac{{\rm d}p(r|{\rm id})}{{\rm d}p(r|{\rm c})} = \frac{1}{2\lambda} e^{\frac{r^2}{2}(2\lambda - 1)},$$

is therefore an effective estimator to distinguish whether individual optical galaxies are true optical counterparts in the tail of the Rayleigh distribution or confusing background sources.

B2   Radio sources with well–defined positions

The likelihood ratio was calculated in this way for every optical galaxy within 5 arcseconds of any single–component radio source, or any radio source with a clear radio core. To investigate the appropriate cut–off value of the likelihood ratio, $LR \geq L$, then (following de Ruiter et al. 1977) the completeness $C(L)$ (the fraction of real identifications which are accepted) and the reliability $R(L)$ (the fraction of accepted identifications which are correct) of the sample can be determined for different values of L according to the equations:

$$C(L) = 1 - \frac{1}{N_{\rm id}} \sum_{LR_i < L} p_i({\rm id}|r)$$

$$R(L) = 1 - \frac{1}{N_{\rm id}} \sum_{LR_i \geq L} p_i({\rm c}|r)$$

where $p_i({\rm id}|r)$ and $p_i({\rm c}|r)$ are the posteriori probabilities for an object found at a normalised distance r to be the true optical counterpart of the radio source or a confusing background object respectively, and $N_{\rm id}$ is the total number of real identifications obtained by summing $p_i({\rm id}|r)$ for all sources. If the a priori probability of finding an optical counterpart to a source is written as $p({\rm id}) = \phi$ then these probabilities can be written as:

$$p_i({\rm id}|{\rm r}) = \frac{\phi LR_i}{\phi LR_i + 1 - \phi}, \qquad p_i({\rm c}|{\rm r}) = \frac{1 - \phi}{\phi LR_i + 1 - \phi}$$

and hence, from ϕ and the values of LR_i, the completeness and the reliability of the sample can be computed as a function of L.

To obtain an estimate of ϕ, for all of the single–component radio sources or those with a clear core, the angular separation between the radio position and the nearest optical galaxy was calculated, and the distribution of these is shown in Figure B1. There is a clear peak of optical objects associated with the radio sources at small angular offsets, with the excess essentially continuing out to about 1 arcsec. 55 of the 87 sources are found within this radius, and a value of $\phi \approx 55/87 = 0.63$ is adopted.

Adopting this value of ϕ, the completeness and reliability of the optical identifications are shown as a function of the likelihood ratio cut–off in Figure B2. The average of these two functions peaks for likelihood ratio cut-offs in the range $0.3 \lesssim L \lesssim 1.2$; a cut-off value of $L = 1$ is therefore adopted. At this value, the completeness of the optical identifications should be $\sim 99\%$ (meaning that for all radio sources whose optical host is bright enough to be detected in the EIS-D catalogue, 99% of them will have been found), and a reliability of over 94%.

B3   Extended radio sources

Where no clear radio core is detected for a double, triple, or multiple component radio source, the source extendness introduces an additional uncertainty into the radio position which must be correctly accounted for in order to accurately estimate the reliability, completeness and identification fraction of the sample.

Table A2. Properties of the radio sources. For each of the sources, the nature of the source (S=single, D=double, T=triple, M=multiple, E=extended diffuse), the integrated and peak flux densities in the new radio observations, the position angle (PA) and largest angular size ($D_{\rm rad}$) of the radio source, and the location and flux of the radio components are all listed. In addition, for each source a "radio source position" is given; for extended sources, this is the location of the radio core, where one is unambiguously detected, or the flux–weighted mean position of the radio emission where no clear core exists. Notes are provided in the text for sources marked with an 'N'.

Name	Morph.	$S_{\rm int}$ (mJy)	PA (°)	$D_{\rm rad}$ ('')	$S_{\rm peak}$ (mJy/bm)	$S_{\rm comp}$ (mJy)	$\alpha_{\rm comp}$ (J2000) (h m s)	$\delta_{\rm comp}$ (° ′ ″)	$\alpha_{\rm sour}$ (J2000) (h m s)	$\delta_{\rm sour}$ (° ′ ″)	Notes
EISD1	D	634.9 ± 1.2	113	5.0	392.3	434.4 ± 0.3	09 51 29.00	−20 50 29.7	09 51 29.07	−20 50 30.1	
					162.9	196.7 ± 0.3	09 51 29.33	−20 50 31.7			
EISD2	S	434.7 ± 1.3	132	0.9	427.0	432.2 ± 0.4	09 46 50.21	−20 20 44.4	09 46 50.21	−20 20 44.4	
EISD3	S	348.7 ± 1.2	130	0.7	340.0	346.4 ± 0.4	09 50 31.39	−21 02 44.8	09 50 31.39	−21 02 44.8	
EISD4	M	221.1 ± 2.5	130	38.4	28.1	34.5 ± 0.2	09 49 04.82	−19 56 58.5	09 49 05.81	−19 57 11.2	
					6.7	119.8 ± 2.5	09 49 05.43	−19 57 07.7			
					24.2	24.1 ± 0.2	09 49 05.81	−19 57 11.2			
					52.3	57.1 ± 0.2	09 49 06.91	−19 57 23.0			
EISD5	T	262.8 ± 2.0	148	14.8	51.2	118.6 ± 0.4	09 59 53.73	−21 48 42.5	09 59 53.99	−21 48 48.3	
					20.8	75.8 ± 0.3	09 59 54.12	−21 48 51.4			
					52.2	68.1 ± 0.2	09 59 54.30	−21 48 55.1			
EISD6	T	230.9 ± 2.1	57	29.5	49.3	60.7 ± 0.2	09 49 52.46	−21 56 28.9	09 49 53.60	−21 56 18.4	
					10.2	24.5 ± 0.3	09 49 52.79	−21 56 24.1			
					82.3	146.7 ± 0.5	09 49 54.24	−21 56 12.9			
EISD7	S	236.2 ± 1.3	53	1.8	196.9	230.5 ± 0.4	09 51 43.63	−21 23 58.0	09 51 43.63	−21 23 58.0	N
EISD8	T	235.3 ± 2.1	145	31.7	154.0	164.6 ± 0.4	09 53 43.67	−21 35 44.5	09 53 44.42	−21 36 02.5	
					0.4	0.4 ± 0.1	09 53 44.42	−21 36 02.5			
					58.0	63.5 ± 0.2	09 53 44.96	−21 36 10.6			
EISD9	D	189.5 ± 1.3	179	8.1	56.7	86.8 ± 0.3	09 58 13.08	−21 44 38.7	09 58 13.08	−21 44 43.0	
					56.5	99.4 ± 0.3	09 58 13.09	−21 44 46.8			
EISD10	M	114.7 ± 2.7	41	32.2	5.6	25.9 ± 0.7	09 45 55.97	−21 17 06.3	09 45 56.71	−21 16 54.4	
					3.3	3.4 ± 0.2	09 45 56.71	−21 16 54.4			
					27.1	30.5 ± 0.3	09 45 57.14	−21 16 48.2			
					24.2	47.6 ± 0.3	09 45 57.48	−21 16 41.9			
EISD11	S	143.5 ± 1.2	61	5.8	91.7	141.6 ± 0.5	09 57 30.07	−21 30 59.8	09 57 30.07	−21 30 59.8	
EISD12	S	109.0 ± 0.3		< 0.6	108.2	109.0 ± 0.3	09 49 35.43	−21 56 23.5	09 49 35.43	−21 56 23.5	
EISD13	S	87.9 ± 1.4	105	2.0	73.4	83.8 ± 0.2	09 44 27.14	−21 16 11.0	09 44 27.14	−21 16 11.0	
EISD14	D	80.8 ± 1.0	121	3.3	35.4	39.4 ± 0.2	09 59 51.06	−20 53 19.0	09 59 51.16	−20 53 19.9	
					39.8	42.6 ± 0.2	09 59 51.26	−20 53 20.7			
EISD15	S	101.1 ± 0.4		< 0.6	100.4	101.1 ± 0.2	09 53 29.51	−20 02 12.5	09 53 29.51	−20 02 12.5	N
EISD16	T	78.2 ± 2.1	176	66.5	2.9	13.6 ± 0.4	09 47 26.86	−21 26 25.1	09 47 26.99	−21 26 22.6	N
					33.9	51.2 ± 0.3	09 47 26.98	−21 26 16.7			
					2.6	7.9 ± 0.3	09 47 27.32	−21 27 21.7			
EISD17	S	79.2 ± 0.4	121	1.3	78.0	79.2 ± 0.2	09 44 33.14	−21 05 08.0	09 44 33.14	−21 05 08.0	
EISD18	S	66.8 ± 1.5	73	1.8	51.7	61.6 ± 0.2	09 46 41.13	−20 29 27.3	09 46 41.13	−20 29 27.3	
EISD19	S	58.8 ± 1.0	85	2.4	46.7	59.5 ± 0.2	09 45 08.38	−20 38 09.1	09 45 08.38	−20 38 09.1	
EISD20	S/T	53.2 ± 2.3	152	2.1/41.3	39.5	50.8 ± 0.3	09 54 28.97	−21 56 55.0	09 54 28.97	−21 56 55.0	N
					0.6	0.6 ± 0.1	09 54 28.09	−21 56 34.0			
					1.5	1.6 ± 0.1	09 54 27.58	−21 56 17.7			
EISD21	D	57.9 ± 1.2	22	10.0	17.5	27.8 ± 0.3	09 54 47.52	−20 59 48.6	09 54 47.66	−20 59 43.8	
					20.6	30.4 ± 0.2	09 54 47.79	−20 59 39.4			
EISD22	D	60.7 ± 1.1	43	6.1	19.1	20.6 ± 0.2	09 46 50.92	−20 53 20.7	09 46 51.12	−20 53 17.8	
					38.3	39.6 ± 0.2	09 46 51.22	−20 53 16.2			
EISD23	D	54.7 ± 1.7	140	13.1	12.4	18.4 ± 0.2	09 57 51.08	−21 33 18.6	09 57 51.42	−21 33 24.2	
					12.4	23.2 ± 0.3	09 57 51.68	−21 33 28.6			
EISD24	D	47.5 ± 1.7	143	11.2	19.4	24.1 ± 0.3	09 52 42.74	−19 58 16.5	09 52 42.95	−19 58 20.4	N
					15.1	19.0 ± 0.3	09 52 43.22	−19 58 25.4			
EISD25	S	59.3 ± 0.8	34	0.8	55.1	56.8 ± 0.3	09 55 13.60	−21 23 03.1	09 55 13.60	−21 23 03.1	N
EISD26	D	55.6 ± 2.2	57	39.9	1.8	2.1 ± 0.2	09 59 02.60	−20 08 27.2	09 59 04.88	−20 08 06.6	
					41.7	48.5 ± 0.2	09 59 04.98	−20 08 05.7			
EISD27	M	51.7 ± 1.6	11	23.9	3.7	8.6 ± 0.5	09 53 30.40	−21 36 11.4	09 53 30.69	−21 35 50.0	
					4.0	10.1 ± 0.4	09 53 30.44	−21 36 05.0			
					3.9	7.0 ± 0.5	09 53 30.48	−21 35 52.6			
					2.4	17.1 ± 0.8	09 53 30.74	−21 35 47.9			
EISD28	S	50.8 ± 0.4		< 1.0	50.6	50.8 ± 0.2	09 47 58.94	−21 21 50.9	09 47 58.94	−21 21 50.9	
EISD29	D	59.6 ± 1.1	3	4.6	29.5	31.6 ± 0.2	09 57 30.92	−21 32 41.6	09 57 30.92	−21 32 39.5	
					23.6	27.1 ± 0.2	09 57 30.93	−21 32 37.0			
EISD30	D	44.0 ± 0.6	163	7.1	41.5	43.2 ± 0.3	09 46 04.74	−21 15 10.7	09 46 04.75	−21 15 11.4	
					0.9	0.8 ± 0.1	09 46 04.58	−21 15 04.0			

Table A2. *continued.* Properties of the radio sources.

Name	Morph.	$S_{\rm int}$ (mJy)	PA (°)	$D_{\rm rad}$ ('')	$S_{\rm peak}$ (mJy/bm)	$S_{\rm comp}$ (mJy)	$\alpha_{\rm comp}$ (J2000) (h m s)	$\delta_{\rm comp}$ (° ′ ″)	$\alpha_{\rm sour}$ (J2000) (h m s)	$\delta_{\rm sour}$ (° ′ ″)	Notes
EISD31	D	44.5 ± 1.2	11	21.7	21.5	27.4 ± 0.4	09 56 29.90	−20 01 39.0	09 56 30.01	−20 01 31.0	
					9.5	16.4 ± 0.5	09 56 30.19	−20 01 17.7			
EISD32	S	48.2 ± 0.8	143	1.4	43.1	48.4 ± 0.3	09 54 38.33	−21 04 25.1	09 54 38.33	−21 04 25.1	
EISD33	D	46.0 ± 1.7	5	37.0	6.0	15.2 ± 0.5	09 54 33.58	−22 05 43.1	09 54 33.70	−22 05 22.3	
					7.0	19.6 ± 0.6	09 54 33.79	−22 05 06.2			
EISD34	S	41.2 ± 0.3		< 0.7	40.6	41.2 ± 0.3	09 48 04.05	−21 47 36.8	09 48 04.05	−21 47 36.8	
EISD35	D	29.8 ± 2.3	131	29.3	9.6	15.7 ± 0.5	09 59 02.22	−20 39 53.6	09 59 02.35	−20 39 51.0	
					0.4	1.5 ± 0.5	09 59 03.50	−20 39 31.0			
EISD36	S	38.7 ± 0.9	82	2.1	34.8	39.3 ± 0.4	09 52 17.69	−20 08 36.2	09 52 17.69	−20 08 36.2	
EISD37	S	36.5 ± 0.4		< 0.8	36.5	36.5 ± 0.4	09 58 26.09	−20 44 52.7	09 58 26.09	−20 44 52.7	
EISD38	T	35.0 ± 2.8	115	17.6	7.7	15.7 ± 0.7	09 46 30.97	−20 26 07.6	09 46 31.32	−20 26 07.2	N
					2.5	2.6 ± 0.2	09 46 31.51	−20 25 46.4			
					5.0	6.3 ± 0.3	09 46 32.11	−20 26 14.9			
EISD39	M	32.5 ± 1.7	157	27.6	3.5	9.8 ± 0.4	09 48 15.54	−21 39 55.8	09 48 15.71	−21 40 06.3	
					10.6	11.4 ± 0.4	09 48 15.71	−21 40 06.3			
					1.1	3.1 ± 0.4	09 48 15.80	−21 40 15.9			
					0.3	1.1 ± 0.3	09 48 16.32	−21 40 21.2			
EISD40	T	23.8 ± 1.4	154	50.1	3.2	11.8 ± 0.4	09 45 55.77	−20 28 13.1	09 45 55.86	−20 28 30.2	
					1.9	4.3 ± 0.4	09 45 55.86	−20 28 30.2			
					2.1	7.3 ± 0.2	09 45 57.29	−20 28 58.4			
EISD41	D	28.6 ± 1.3	1	28.5	13.9	17.6 ± 0.3	09 45 19.59	−21 42 50.7	09 45 19.60	−21 42 43.8	
					4.7	5.7 ± 0.3	09 45 19.62	−21 42 22.2			
EISD42	S	38.6 ± 1.0	24	0.6	35.5	36.4 ± 0.2	09 58 27.58	−21 05 27.5	09 58 27.58	−21 05 27.5	
EISD43	D	21.2 ± 1.5	100	36.3	4.5	5.9 ± 0.4	09 51 39.63	−20 11 15.1	09 51 41.02	−20 11 18.4	
					4.5	8.5 ± 0.4	09 51 42.17	−20 11 21.2			
EISD44	M	18.8 ± 1.7	146	115.2	2.3	3.1 ± 0.2	09 51 46.97	−21 24 01.9	09 51 49.78	−21 24 57.7	N
					0.7	1.2 ± 0.1	09 51 47.21	−21 24 16.4			
					0.4	0.5 ± 0.1	09 51 49.78	−21 24 57.7			
					1.2	6.4 ± 0.3	09 51 50.02	−21 25 25.2			
					2.9	4.6 ± 0.2	09 51 51.60	−21 25 37.1			
EISD45	D	33.6 ± 1.4	144	23.2	21.4	24.6 ± 0.3	09 53 04.59	−20 44 07.5	09 53 04.71	−20 44 09.8	
					1.5	3.5 ± 0.5	09 53 05.56	−20 44 26.2			
EISD46	D	30.3 ± 1.2	105	6.7	9.2	11.7 ± 0.3	09 44 55.10	−20 17 12.0	09 44 55.38	−20 17 13.1	
					11.9	17.9 ± 0.4	09 44 55.56	−20 17 13.7			
EISD47	S	27.4 ± 0.4		< 0.9	27.3	27.4 ± 0.4	09 47 53.55	−21 47 19.6	09 47 53.55	−21 47 19.6	
EISD48	D	23.9 ± 1.2	64	12.2	6.6	11.7 ± 0.5	09 54 52.06	−21 19 31.5	09 54 52.43	−21 19 29.0	
					5.5	10.7 ± 0.5	09 54 52.85	−21 19 26.3			
EISD49	D	31.9 ± 2.9	55	61.3	1.8	12.3 ± 1.4	09 59 24.16	−20 06 57.9	09 59 24.91	−20 06 50.4	
					1.7	3.3 ± 0.5	09 59 27.73	−20 06 22.8			
EISD50	S	34.3 ± 0.3		< 0.7	34.4	34.3 ± 0.3	09 57 24.17	−22 03 53.4	09 57 24.17	−22 03 53.4	
EISD51	S	34.0 ± 1.0	113	0.7	31.6	32.7 ± 0.3	09 49 33.23	−21 27 08.3	09 49 33.23	−21 27 08.3	
EISD52	T	26.5 ± 1.3	90	21.3	6.2	11.0 ± 0.5	09 49 18.76	−21 51 35.6	09 49 19.44	−21 51 35.4	
					3.3	6.0 ± 0.5	09 49 19.75	−21 51 35.0			
					5.5	6.6 ± 0.4	09 49 20.29	−21 51 35.6			
EISD53	S	32.6 ± 1.0	70	3.4	21.3	30.8 ± 0.5	09 51 16.77	−20 56 38.4	09 51 16.77	−20 56 38.4	
EISD54	D	25.1 ± 1.0	50	6.4	8.5	9.8 ± 0.3	09 48 35.79	−21 06 25.0	09 48 35.99	−21 06 22.6	
					11.7	13.2 ± 0.4	09 48 36.14	−21 06 20.9			
EISD55	D	23.5 ± 0.5	134	11.3	22.0	22.9 ± 0.3	09 50 58.61	−21 14 19.8	09 50 58.63	−21 14 20.3	
					0.4	0.4 ± 0.1	09 50 59.19	−21 14 27.7			
EISD56	D	10.5 ± 0.8	174	12.6	3.4	6.4 ± 0.4	09 47 28.10	−21 28 53.3	09 47 28.14	−21 28 57.9	N
					2.6	3.9 ± 0.2	09 47 28.21	−21 29 05.8			
EISD57	S	25.5 ± 1.6	49	23.5	19.8	20.3 ± 0.4	09 58 16.61	−20 18 59.2	09 58 16.61	−20 18 59.2	
EISD58	T	26.8 ± 1.9	163	42.2	2.1	6.7 ± 0.7	09 49 17.95	−20 54 30.4	09 49 18.18	−20 54 45.4	
					1.6	8.1 ± 1.1	09 49 18.18	−20 54 45.4			
					1.6	2.1 ± 0.2	09 49 18.86	−20 55 10.7			
EISD59	S	26.7 ± 0.4		< 1.2	26.8	26.7 ± 0.4	09 44 53.53	−20 46 37.3	09 44 53.53	−20 46 37.3	
EISD60	D	24.6 ± 1.2	74	18.2	8.0	10.1 ± 0.3	09 52 01.58	−21 15 53.6	09 52 01.86	−21 15 52.3	
					6.3	10.1 ± 0.4	09 52 02.14	−21 15 50.9			
EISD61	D	6.0 ± 0.7	126	38.1	0.7	0.9 ± 0.2	09 59 38.41	−20 34 22.6	09 59 40.04	−20 34 38.7	
					2.3	2.8 ± 0.3	09 59 40.56	−20 34 44.5			
EISD62	S	31.1 ± 0.3		< 1.1	30.2	31.1 ± 0.3	09 54 27.06	−20 29 46.5	09 54 27.06	−20 29 46.5	
EISD63	D	19.1 ± 1.1	118	9.0	3.5	10.6 ± 0.6	09 47 03.06	−20 50 00.3	09 47 03.32	−20 50 02.2	
					4.2	8.7 ± 0.6	09 47 03.63	−20 50 04.5			

Table A2. *continued.* Properties of the radio sources.

Name	Morph.	$S_{\rm int}$ (mJy)	PA (°)	$D_{\rm rad}$ ($''$)	$S_{\rm peak}$ (mJy/bm)	$S_{\rm comp}$ (mJy)	$\alpha_{\rm comp}$ (J2000) (h m s)	$\delta_{\rm comp}$ (° ′ ″)	$\alpha_{\rm sour}$ (J2000) (h m s)	$\delta_{\rm sour}$ (° ′ ″)	Notes
EISD64	D	18.3 ± 1.0	153	5.7	8.5	10.9 ± 0.4	09 52 59.10	-21 48 40.3	09 52 59.17	-21 48 42.4	
					5.8	7.4 ± 0.4	09 52 59.28	-21 48 45.4			
EISD65	S	21.2 ± 0.3		< 1.1	21.0	21.2 ± 0.3	09 54 03.02	-20 25 13.2	09 54 03.02	-20 25 13.2	
EISD66	S	23.6 ± 1.0	161	6.2	7.6	23.1 ± 0.5	09 57 42.91	-20 06 36.1	09 57 42.91	-20 06 36.1	
EISD67	S	26.0 ± 0.3		< 1.0	25.5	26.0 ± 0.3	09 53 23.18	-20 13 43.5	09 53 23.18	-20 13 43.5	
EISD68	S	24.2 ± 1.1	7	1.4	17.7	19.9 ± 0.4	09 54 28.28	-20 39 26.6	09 54 28.28	-20 39 26.6	
EISD69	D	19.4 ± 1.0	104	5.0	6.9	7.5 ± 0.4	09 52 12.50	-21 02 35.6	09 52 12.71	-21 02 36.3	
					8.7	10.8 ± 0.3	09 52 12.85	-21 02 36.8			
EISD70	D	19.0 ± 1.7	108	35.3	2.1	2.3 ± 0.2	09 51 28.36	-22 04 18.4	09 51 30.48	-22 04 28.1	
					16.9	17.7 ± 0.3	09 51 30.77	-22 04 29.4			
EISD71	D	16.6 ± 1.0	72	14.0	8.1	9.9 ± 0.4	09 49 30.24	-20 23 35.8	09 49 30.56	-20 23 34.2	
					1.9	5.2 ± 0.8	09 49 31.18	-20 23 31.3			
EISD72	S	23.4 ± 0.3		< 1.2	24.0	23.4 ± 0.3	09 45 42.64	-21 15 44.9	09 45 42.64	-21 15 44.9	
EISD73									09 55 46.10	-21 26 55.6	N
EISD74	S	15.9 ± 0.6		< 2.3	13.8	15.9 ± 0.6	09 53 20.56	-21 43 59.2	09 53 20.56	-21 43 59.2	
EISD75	D	17.4 ± 0.9	29	5.8	15.8	15.6 ± 0.3	09 51 22.87	-21 51 55.5	09 51 22.89	-21 51 55.1	
					1.7	1.2 ± 0.3	09 51 23.08	-21 51 50.4			
EISD76	D	24.6 ± 1.7	69	10.9	6.2	8.8 ± 0.4	09 51 32.02	-21 00 31.6	09 51 32.40	-21 00 29.6	
					4.3	9.4 ± 0.5	09 51 32.74	-21 00 27.7			
EISD77									09 55 23.78	-21 28 30.5	N
EISD78	D	20.2 ± 1.3	13	20.4	4.4	9.3 ± 0.5	09 50 43.08	-21 26 47.8	09 50 43.20	-21 26 40.7	
					3.8	5.2 ± 0.4	09 50 43.41	-21 26 27.9			
EISD79	S	18.6 ± 0.4		< 1.7	16.9	18.6 ± 0.4	09 48 55.25	-21 03 55.6	09 48 55.25	-21 03 55.6	
EISD80	D	13.3 ± 1.6	26	22.5	4.4	8.4 ± 0.5	09 51 20.69	-21 30 04.7	09 51 21.02	-21 29 55.4	
					3.8	7.1 ± 0.5	09 51 21.40	-21 29 44.5			
EISD81	T	4.3 ± 1.1	21	33.1	0.9	1.2 ± 0.1	09 48 42.09	-21 52 39.5	09 48 42.44	-21 52 24.8	
					0.5	0.6 ± 0.1	09 48 42.44	-21 52 24.8			
					0.3	0.6 ± 0.1	09 48 42.94	-21 52 08.7			
EISD82	D	9.5 ± 1.3	114	21.3	5.8	6.3 ± 0.2	09 48 01.25	-20 09 07.6	09 48 01.87	-20 09 11.4	
					3.9	5.0 ± 0.3	09 48 02.64	-20 09 16.2			
EISD83	S	17.8 ± 0.3		< 0.8	17.6	17.8 ± 0.3	09 51 48.66	-20 31 52.9	09 51 48.66	-20 31 52.9	
EISD84	D	14.8 ± 1.3	97	17.7	3.6	9.4 ± 0.5	09 49 45.24	-21 50 05.4	09 49 45.67	-21 50 06.2	
					3.0	4.8 ± 0.5	09 49 46.50	-21 50 07.7			
EISD85	S	11.9 ± 0.7	179	6.5	6.2	11.9 ± 0.2	09 48 59.78	-20 50 08.5	09 48 59.78	-20 50 08.5	
EISD86									09 55 12.44	-21 23 09.6	N
EISD87	S	14.7 ± 1.4	62	7.3	7.9	14.4 ± 0.8	09 57 26.04	-20 13 05.7	09 57 26.04	-20 13 05.7	
EISD88	D	12.3 ± 1.1	169	6.3	5.1	9.8 ± 0.2	09 45 29.50	-21 18 49.7	09 45 29.51	-21 18 50.5	
					0.9	1.2 ± 0.3	09 45 29.58	-21 18 55.9			
EISD89	T	16.6 ± 1.6	77	38.8	1.6	7.2 ± 0.5	09 57 31.17	-21 20 29.7	09 57 31.87	-21 20 26.7	
					1.9	6.6 ± 0.4	09 57 32.41	-21 20 25.6			
					0.9	1.2 ± 0.1	09 57 33.54	-21 20 17.1			
EISD90	S	17.4 ± 1.7	75	7.1	4.4	12.9 ± 1.0	09 50 46.38	-21 32 55.1	09 50 46.38	-21 32 55.1	
EISD91	S	13.9 ± 0.3		< 0.9	13.7	13.9 ± 0.2	09 54 51.96	-21 30 16.1	09 54 51.96	-21 30 16.1	
EISD92	S	15.7 ± 0.3		< 1.4	15.0	15.7 ± 0.2	09 56 02.36	-21 56 04.2	09 56 02.36	-21 56 04.2	
EISD93	S	12.7 ± 0.3		< 3.5	10.2	12.7 ± 0.2	09 55 41.89	-20 39 39.2	09 55 41.89	-20 39 39.2	
EISD94	T	22.3 ± 1.2	153	15.8	4.7	6.0 ± 0.3	09 56 27.88	-20 48 37.9	09 56 28.10	-20 48 45.3	
					0.4	0.4 ± 0.1	09 56 28.10	-20 48 45.3			
					7.4	11.1 ± 0.4	09 56 28.38	-20 48 52.1			
EISD95	D	15.6 ± 1.5	42	23.9	9.5	10.1 ± 0.3	09 44 28.62	-20 38 04.3	09 44 28.90	-20 37 59.9	
					2.4	3.4 ± 0.2	09 44 29.74	-20 37 46.5			
EISD96	S	15.7 ± 1.2	66	2.5	9.4	13.1 ± 0.4	09 49 29.75	-21 29 38.6	09 49 29.75	-21 29 38.6	
EISD97	S	19.1 ± 0.3		< 0.7	18.9	19.1 ± 0.3	09 49 25.99	-20 37 24.2	09 49 25.99	-20 37 24.2	
EISD98	D	10.4 ± 1.2	148	10.9	0.6	3.1 ± 0.6	09 45 26.76	-20 33 51.5	09 45 26.97	-20 33 55.0	N
					2.4	3.3 ± 0.3	09 45 27.17	-20 33 57.7			
EISD99	D	10.7 ± 1.8	119	12.3	3.4	5.3 ± 0.3	09 44 46.45	-20 49 57.4	09 44 46.77	-20 49 59.9	
					3.1	3.6 ± 0.2	09 44 47.22	-20 50 03.4			
EISD100	S	11.6 ± 0.3		< 1.8	10.6	11.6 ± 0.3	09 58 43.94	-20 51 32.3	09 58 43.94	-20 51 32.3	
EISD101	S	11.9 ± 0.3		< 1.5	12.3	11.9 ± 0.3	09 58 44.87	-20 31 18.1	09 58 44.87	-20 31 18.1	
EISD102	D	23.6 ± 1.4	149	10.9	1.6	7.3 ± 0.6	09 57 45.68	-21 23 18.7	09 57 45.89	-21 23 23.6	
					6.1	8.1 ± 0.4	09 57 46.08	-21 23 28.0			
EISD103	D	8.4 ± 1.3	78	45.9	3.7	3.5 ± 0.2	09 55 43.52	-21 25 27.8	09 55 45.19	-21 25 23.0	N
					1.0	3.1 ± 0.4	09 55 46.67	-21 25 18.7			
EISD104	S	12.7 ± 0.3		< 2.2	10.9	12.7 ± 0.3	09 49 42.98	-20 37 45.5	09 49 42.98	-20 37 45.5	

**Table A2.** *continued.* Properties of the radio sources.

Name	Morph.	$S_{\rm int}$ (mJy)	PA (°)	$D_{\rm rad}$ ('')	$S_{\rm peak}$ (mJy/bm)	$S_{\rm comp}$ (mJy)	$\alpha_{\rm comp}$ (J2000) (h m s)	$\delta_{\rm comp}$ (° ' '')	$\alpha_{\rm sour}$ (J2000) (h m s)	$\delta_{\rm sour}$ (° ' '')	Notes
EISD105	D	16.4 ± 2.1	158	40.1	1.7	4.2 ± 0.6	09 54 15.95	−21 28 45.1	09 54 16.43	−21 29 01.6	
					1.2	3.4 ± 0.6	09 54 17.02	−21 29 22.3			
EISD106	S	11.8 ± 0.8	154	5.3	6.3	8.7 ± 0.4	09 45 48.48	−21 59 06.1	09 45 48.48	−21 59 06.1	
EISD107	D	16.0 ± 1.1	177	6.9	3.4	8.0 ± 0.6	09 55 59.22	−20 42 48.8	09 55 59.23	−20 42 51.6	
					3.0	5.3 ± 0.4	09 55 59.24	−20 42 55.7			
EISD108	D	6.9 ± 0.6	29	33.4	2.7	6.1 ± 0.4	09 57 42.32	−19 56 00.9	09 57 42.23	−19 56 02.8	
					0.3	0.4 ± 0.1	09 57 41.16	−19 56 30.0			
EISD109	D	6.9 ± 0.9	110	8.5	2.0	4.1 ± 0.4	09 44 46.73	−20 58 22.0	09 44 46.93	−20 58 23.1	
					1.7	2.3 ± 0.3	09 44 47.30	−20 58 25.0			
EISD110	S	11.1 ± 0.9	82	10.9	2.7	8.7 ± 0.5	09 54 53.26	−21 15 12.9	09 54 53.26	−21 15 12.9	
EISD111	D	7.7 ± 1.2	115	9.4	2.2	2.7 ± 0.2	09 45 55.71	−21 20 53.3	09 45 56.03	−21 20 51.0	
					0.8	2.9 ± 0.2	09 45 56.31	−21 20 49.9			
EISD112	D	9.8 ± 1.1	37	34.4	1.4	6.8 ± 0.4	09 55 23.77	−21 29 58.8	09 55 23.82	−21 29 57.2	N
					0.2	0.3 ± 0.1	09 55 25.28	−21 29 31.6			
EISD113	D	18.1 ± 1.4	113	22.1	3.3	3.3 ± 0.4	09 50 53.72	−21 33 08.6	09 50 53.62	−21 33 07.5	
					0.3	0.4 ± 0.1	09 50 52.25	−21 32 59.4			
EISD114	S	11.9 ± 0.4		< 3.1	8.3	11.9 ± 0.4	09 47 34.47	−21 26 58.0	09 47 34.47	−21 26 58.0	N
EISD115	S	9.3 ± 0.3		< 2.7	9.4	9.3 ± 0.3	09 44 45.31	−21 46 23.7	09 44 45.31	−21 46 23.7	
EISD116	S	13.6 ± 0.3		< 1.2	14.1	13.6 ± 0.3	09 51 29.69	−20 16 42.8	09 51 29.69	−20 16 42.8	
EISD117	T	10.8 ± 1.3	72	18.9	2.2	4.1 ± 0.3	09 53 08.65	−20 01 24.1	09 53 09.24	−20 01 21.3	
					1.4	1.8 ± 0.2	09 53 09.44	−20 01 20.3			
					1.6	3.2 ± 0.3	09 53 09.92	−20 01 18.2			
EISD118									09 57 24.26	−21 29 43.3	N
EISD119	S	12.0 ± 0.8	123	2.3	9.0	10.5 ± 0.3	09 45 20.95	−22 01 22.2	09 45 20.95	−22 01 22.2	
EISD120	S	11.8 ± 0.3		< 1.3	12.2	11.8 ± 0.2	09 48 04.20	−20 34 34.8	09 48 04.20	−20 34 34.8	
EISD121	D	6.6 ± 1.2	159	29.1	1.9	2.6 ± 0.2	09 54 56.54	−22 04 59.2	09 54 56.87	−22 05 10.9	
					1.5	2.0 ± 0.2	09 54 57.30	−22 05 26.3			
EISD122	T	12.9 ± 1.4	20	94.1	1.3	3.7 ± 0.1	09 52 55.18	−20 52 19.3	09 52 55.92	−20 51 45.4	
					3.1	3.3 ± 0.3	09 52 55.92	−20 51 45.4			
					1.4	3.3 ± 0.3	09 52 57.55	−20 50 51.2			
EISD123	S	6.8 ± 0.8	45	1.6	4.8	6.3 ± 0.3	09 54 21.48	−21 48 07.2	09 54 21.48	−21 48 07.2	
EISD124	M	12.4 ± 0.7	10	154.3	1.0	1.6 ± 0.1	09 48 10.13	−20 02 00.4	09 48 10.91	−20 00 59.9	N
					0.4	2.4 ± 0.5	09 48 10.24	−20 01 53.6			
					1.2	1.7 ± 0.1	09 48 11.83	−19 59 28.0			
					0.3	1.1 ± 0.5	09 48 12.06	−19 59 56.8			
EISD125	S	10.4 ± 0.9	129	8.5	5.4	11.0 ± 0.5	09 45 21.12	−20 43 21.4	09 45 21.12	−20 43 21.4	
EISD126	D	7.7 ± 2.0	10	51.8	1.4	3.0 ± 0.5	09 54 35.99	−21 44 54.2	09 54 36.32	−21 44 26.6	
					1.3	3.5 ± 0.6	09 54 36.60	−21 44 03.1			
EISD127	S	10.7 ± 0.3		< 1.3	11.4	10.7 ± 0.3	09 48 22.16	−21 05 08.9	09 48 22.16	−21 05 08.9	
EISD128	T?	1.9 ± 0.7	115	43.1	0.3	0.4 ± 0.1	09 58 14.71	−20 58 18.8	09 58 16.37	−20 58 19.4	
					0.2	0.4 ± 0.1	09 58 14.81	−20 58 10.5			
					0.4	0.6 ± 0.1	09 58 17.59	−20 58 28.5			
EISD129	S	10.3 ± 0.4		< 2.6	7.9	10.3 ± 0.4	09 56 20.42	−22 03 50.5	09 56 20.42	−22 03 50.5	
EISD130	S	9.4 ± 0.3		< 1.1	9.7	9.4 ± 0.2	09 49 35.13	−21 58 10.5	09 49 35.13	−21 58 10.5	
EISD131	S	11.5 ± 0.3		< 1.0	11.4	11.5 ± 0.2	09 49 25.99	−20 05 20.2	09 49 25.99	−20 05 20.2	
EISD132	D	9.5 ± 1.1	106	14.5	1.7	5.7 ± 0.6	09 46 18.63	−20 37 56.6	09 46 18.86	−20 37 57.4	
					0.4	1.4 ± 0.5	09 46 19.62	−20 38 00.7			
EISD133	S	6.8 ± 0.8	44	4.0	2.9	3.9 ± 0.4	09 57 02.25	−21 56 51.8	09 57 02.25	−21 56 51.8	
EISD134	D	7.3 ± 0.4	48	12.0	0.4	1.7 ± 0.1	09 46 49.44	−21 16 45.4	09 46 49.27	−21 16 48.7	
					0.3	0.8 ± 0.1	09 46 48.90	−21 16 55.0			
EISD135	S	9.5 ± 0.3		< 2.0	9.8	9.5 ± 0.3	09 58 51.76	−21 10 23.0	09 58 51.76	−21 10 23.0	
EISD136	S	13.4 ± 0.9	57	4.7	6.7	11.7 ± 0.3	09 50 48.57	−21 54 57.1	09 50 48.57	−21 54 57.1	
EISD137	S	5.7 ± 0.3		< 6.8	3.9	5.7 ± 0.3	09 48 14.15	−19 59 56.0	09 48 14.15	−19 59 56.0	N
EISD138	S	9.0 ± 0.4		< 6.8	5.7	9.0 ± 0.3	09 47 24.38	−21 05 02.3	09 47 24.38	−21 05 02.3	
EISD139	S	10.8 ± 0.3		< 3.0	7.9	10.8 ± 0.3	09 52 50.38	−21 31 48.0	09 52 50.38	−21 31 48.0	
EISD140	S	4.2 ± 0.6	20	5.5	2.5	3.6 ± 0.4	09 59 33.76	−21 14 54.6	09 59 33.76	−21 14 54.6	
EISD141	T	6.2 ± 0.3	167	83.4	0.4	1.0 ± 0.2	09 55 11.38	−20 29 14.8	09 55 11.49	−20 30 18.7	
					1.1	3.0 ± 0.2	09 55 11.49	−20 30 18.7			
					0.9	2.2 ± 0.3	09 55 12.69	−20 30 36.1			
EISD142	S	10.9 ± 0.9	116	5.6	2.8	8.8 ± 0.5	09 56 06.94	−20 05 43.8	09 56 06.94	−20 05 43.8	
EISD143	S	7.9 ± 0.3		< 1.3	8.0	7.9 ± 0.2	09 57 35.35	−20 29 35.4	09 57 35.35	−20 29 35.4	
EISD144	S	9.0 ± 0.5		< 3.3	6.8	9.0 ± 0.3	09 44 50.69	−20 17 36.1	09 44 50.69	−20 17 36.1	

Table A2. *continued.* Properties of the radio sources.

Name	Morph.	S_{int} (mJy)	PA (°)	D_{rad} ('')	S_{peak} (mJy/bm)	S_{comp} (mJy)	α_{comp} (J2000) (h m s)	δ_{comp} (° ′ ″)	α_{sour} (J2000) (h m s)	δ_{sour} (° ′ ″)	Notes
EISD145	D	9.2 ± 1.3	127	31.8	1.5	1.8 ± 0.2	09 57 38.30	-20 03 10.1	09 57 39.51	-20 03 22.6	
					2.4	3.5 ± 0.4	09 57 40.12	-20 03 29.0			
EISD146	S	10.4 ± 0.3		< 1.1	10.1	10.4 ± 0.2	09 56 42.31	-21 19 44.6	09 56 42.31	-21 19 44.6	
EISD147	T	3.5 ± 0.7	16	8.6	0.5	0.9 ± 0.3	09 58 57.19	-20 34 14.3	09 58 57.26	-20 34 10.4	
					0.5	0.5 ± 0.2	09 58 57.26	-20 34 10.4			
					0.4	0.9 ± 0.3	09 58 57.35	-20 34 06.0			
EISD148	D	3.9 ± 0.4	89	7.0	1.4	2.5 ± 0.2	09 45 37.59	-21 11 14.2	09 45 37.77	-21 11 14.2	
					1.1	1.4 ± 0.1	09 45 38.09	-21 11 14.1			
EISD149	S	7.7 ± 0.8	49	2.3	4.6	6.4 ± 0.3	09 47 44.76	-21 12 23.6	09 47 44.76	-21 12 23.6	
EISD150	D	13.8 ± 1.2	95	19.7	2.4	7.3 ± 0.5	09 47 09.55	-20 35 52.3	09 47 10.01	-20 35 52.8	
					1.6	3.5 ± 0.4	09 47 10.95	-20 35 54.0			
EISD151									09 55 53.71	-21 27 12.1	N
EISD152	S	9.3 ± 0.5		< 5.1	4.3	9.3 ± 0.5	09 59 27.68	-20 03 17.1	09 59 27.68	-20 03 17.1	
EISD153	S	10.3 ± 0.3		< 1.3	9.6	10.3 ± 0.3	09 56 49.76	-20 35 25.9	09 56 49.76	-20 35 25.9	
EISD154	S	4.9 ± 0.5		< 3.9	3.0	4.9 ± 0.5	09 52 10.91	-20 50 11.2	09 52 10.91	-20 50 11.2	
EISD155	D	7.6 ± 1.0	173	13.1	1.2	3.0 ± 0.6	09 57 24.88	-20 22 42.5	09 57 24.93	-20 22 48.0	
					1.4	2.1 ± 0.4	09 57 25.00	-20 22 55.5			
EISD156	T	3.8 ± 0.7	163	28.4	0.6	1.6 ± 0.2	09 56 36.81	-20 18 55.0	09 56 37.11	-20 19 05.5	
					0.6	0.6 ± 0.1	09 56 37.11	-20 19 05.5			
					0.4	0.8 ± 0.2	09 56 37.36	-20 19 17.4			
EISD157	S	7.3 ± 0.8	104	7.9	4.0	8.5 ± 0.5	09 49 02.22	-21 15 05.5	09 49 02.22	-21 15 05.5	
EISD158	D	5.4 ± 0.7	87	6.0	2.0	2.8 ± 0.3	09 44 43.45	-21 44 37.1	09 44 43.55	-21 44 37.1	
					0.8	1.4 ± 0.4	09 44 43.87	-21 44 36.8	09 44 43.55	-21 44 37.1	
EISD159	S	7.3 ± 0.2		< 1.2	7.1	7.3 ± 0.2	09 53 57.38	-20 36 51.3	09 53 57.38	-20 36 51.3	
EISD160	S	7.5 ± 0.3		< 1.2	7.6	7.5 ± 0.3	09 58 49.71	-21 17 37.1	09 58 49.71	-21 17 37.1	
EISD161	S	8.3 ± 0.7	157	3.7	6.1	9.1 ± 0.3	09 47 48.55	-20 48 34.0	09 47 48.55	-20 48 34.0	
EISD162	S	2.5 ± 0.4		< 3.8	2.2	2.5 ± 0.2	09 56 39.20	-20 10 43.6	09 56 39.20	-20 10 43.6	
EISD163	E	3.4 ± 2.1	4.7	24.8	0.4	2.1 ± 0.6	09 49 10.88	-20 21 53.0	09 49 10.88	-20 21 53.0	
EISD164	S	7.6 ± 0.3		< 0.9	7.9	7.6 ± 0.2	09 52 01.20	-20 24 56.5	09 52 01.20	-20 24 56.5	
EISD165	D	8.7 ± 0.9	71	5.6	3.4	4.4 ± 0.3	09 54 10.35	-21 58 01.8	09 54 10.54	-21 58 00.9	
					4.1	4.2 ± 0.2	09 54 10.73	-21 57 60.0			
EISD166	S	10.9 ± 0.3		< 1.8	11.5	10.9 ± 0.2	09 56 04.45	-21 44 36.7	09 56 04.45	-21 44 36.7	
EISD167	S	6.1 ± 0.3		< 2.7	5.6	6.1 ± 0.2	09 46 02.36	-21 51 44.2	09 46 02.36	-21 51 44.2	
EISD168	S	6.6 ± 0.4		< 1.2	6.6	6.6 ± 0.2	09 44 50.11	-20 07 38.3	09 44 50.11	-20 07 38.3	
EISD169	D	5.6 ± 0.8	13	9.5	1.4	2.7 ± 0.3	09 51 48.87	-21 33 46.2	09 51 48.94	-21 33 41.6	
					1.5	2.7 ± 0.3	09 51 49.03	-21 33 37.0			
EISD170	S	5.7 ± 0.3		< 2.1	5.3	5.7 ± 0.2	09 52 26.51	-20 01 07.1	09 52 26.51	-20 01 07.1	
EISD171	D	6.7 ± 1.3	76	38.3	1.0	2.4 ± 0.4	09 47 49.10	-21 42 13.4	09 47 50.58	-21 42 08.2	
					2.2	3.0 ± 0.3	09 47 51.77	-21 42 04.1			
EISD172	S	6.3 ± 0.3		< 1.2	6.4	6.3 ± 0.2	09 57 22.18	-21 01 06.0	09 57 22.18	-21 01 06.0	
EISD173	S	8.7 ± 0.3		< 1.2	8.7	8.7 ± 0.2	09 54 31.06	-20 35 38.0	09 54 31.06	-20 35 38.0	
EISD174	S	8.5 ± 0.3		< 1.3	8.7	8.5 ± 0.2	09 49 02.78	-20 16 11.5	09 49 02.78	-20 16 11.5	
EISD175	D	8.3 ± 1.1	28	11.8	1.8	3.0 ± 0.3	09 49 22.11	-21 18 24.6	09 49 22.31	-21 18 19.4	
					1.6	3.0 ± 0.3	09 49 22.52	-21 18 14.2			
EISD176									09 58 20.40	-21 39 13.3	N
EISD177	S	6.8 ± 0.8	60	4.4	1.5	3.0 ± 0.4	09 55 26.95	-20 46 06.0	09 55 26.95	-20 46 06.0	
EISD178	D	3.5 ± 0.8	42	10.4	1.2	1.2 ± 0.2	09 47 47.95	-21 00 46.2	09 47 48.33	-21 00 40.4	
					3.9	3.5 ± 0.2	09 47 48.45	-21 00 38.4			
EISD179	S	7.5 ± 0.3		< 1.0	7.8	7.5 ± 0.2	09 49 59.72	-21 27 19.0	09 49 59.72	-21 27 19.0	
EISD180	S	2.8 ± 0.3		< 2.8	2.2	2.8 ± 0.2	09 49 12.72	-22 00 23.4	09 49 12.72	-22 00 23.4	
EISD181	S	4.2 ± 0.4		< 3.8	3.7	4.2 ± 0.2	09 54 41.85	-20 49 43.0	09 54 41.85	-20 49 43.0	
EISD182	D	10.1 ± 1.2	125	22.4	1.2	2.4 ± 0.3	09 49 48.06	-21 34 24.4	09 49 49.00	-21 34 33.7	
					3.9	6.0 ± 0.3	09 49 49.37	-21 34 37.4			
EISD183	D	3.7 ± 0.5	151	11.4	1.4	2.3 ± 0.3	09 51 29.23	-20 25 31.2	09 51 29.36	-20 25 34.6	
					0.6	1.2 ± 0.2	09 51 29.62	-20 25 41.2			
EISD184	S	5.9 ± 0.7	68	4.4	2.4	5.1 ± 0.4	09 45 07.54	-21 09 25.8	09 45 07.54	-21 09 25.8	
EISD185	S	2.2 ± 0.3		< 2.9	1.2	1.5 ± 0.2	09 52 14.34	-21 40 19.0	09 52 14.34	-21 40 19.0	
EISD186	S	9.1 ± 0.3		< 1.0	9.4	9.1 ± 0.2	09 49 24.64	-21 11 12.0	09 49 24.64	-21 11 12.0	
EISD187	D	3.4 ± 0.5	159	33.0	0.9	1.5 ± 0.3	09 50 38.44	-21 40 55.3	09 50 38.80	-21 41 08.4	
					0.9	1.1 ± 0.2	09 50 39.29	-21 41 26.1			
EISD188	S	5.2 ± 0.3		< 1.7	5.1	5.2 ± 0.2	09 47 46.12	-21 27 51.2	09 47 46.12	-21 27 51.2	
EISD189	S	6.7 ± 0.3		< 1.2	6.9	6.7 ± 0.2	09 45 51.03	-20 14 46.9	09 45 51.03	-20 14 46.9	
EISD190	S	6.3 ± 0.2		< 1.6	6.9	6.3 ± 0.2	09 59 37.64	-20 38 26.0	09 59 37.64	-20 38 26.0	

Table A2. *continued.* Properties of the radio sources.

Name	Morph.	$S_{\rm int}$ (mJy)	PA (°)	$D_{\rm rad}$ ('')	$S_{\rm peak}$ (mJy/bm)	$S_{\rm comp}$ (mJy)	$\alpha_{\rm comp}$ (J2000) (h m s)	$\delta_{\rm comp}$ (° ′ ″)	$\alpha_{\rm sour}$ (J2000) (h m s)	$\delta_{\rm sour}$ (° ′ ″)	Notes
EISD191	E	0.7 ± 0.4			0.5	0.6 ± 0.3	09 50 27.68	-21 48 08.7	09 50 27.68	-21 48 08.7	
EISD192	S	4.4 ± 0.3		< 2.1	3.8	4.4 ± 0.3	09 59 12.53	-20 12 53.2	09 59 12.53	-20 12 53.2	
EISD193	S	3.9 ± 0.4		< 2.5	3.7	3.9 ± 0.3	09 50 55.91	-19 55 12.0	09 50 55.91	-19 55 12.0	
EISD194	D	1.9 ± 0.4	29	23.1	0.7	1.0 ± 0.2	09 45 27.39	-20 57 44.1	09 45 27.69	-20 57 35.2	
					0.3	0.6 ± 0.2	09 45 28.18	-20 57 23.9			
EISD195	S	5.2 ± 0.3		< 1.9	5.6	5.2 ± 0.3	09 57 15.56	-20 30 34.8	09 57 15.56	-20 30 34.8	
EISD196									09 50 02.94	-22 05 34.9	N
EISD197	S	4.7 ± 0.3		< 1.7	4.2	4.7 ± 0.3	09 45 21.73	-20 36 00.3	09 45 21.73	-20 36 00.3	
EISD198	S	6.3 ± 0.7	151	1.7	4.2	5.5 ± 0.3	09 58 50.93	-21 08 18.3	09 58 50.93	-21 08 18.3	
EISD199	S	5.1 ± 0.2		< 1.1	5.2	5.1 ± 0.2	09 45 26.34	-21 55 00.4	09 45 26.34	-21 55 00.4	
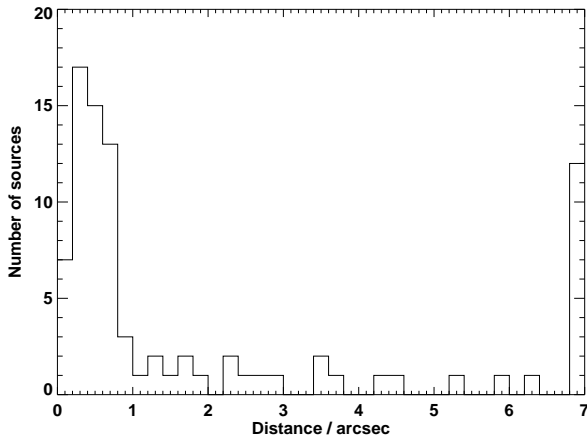
Figure B1. A histogram of angular offsets from the radio source to the nearest object in the EIS catalogue, for all radio sources whose central position is clearly defined, either as a single–component radio sources or a source with a clear core. The last bin also contains those sources for which the nearest object is more than 7 arcsec from the radio position.
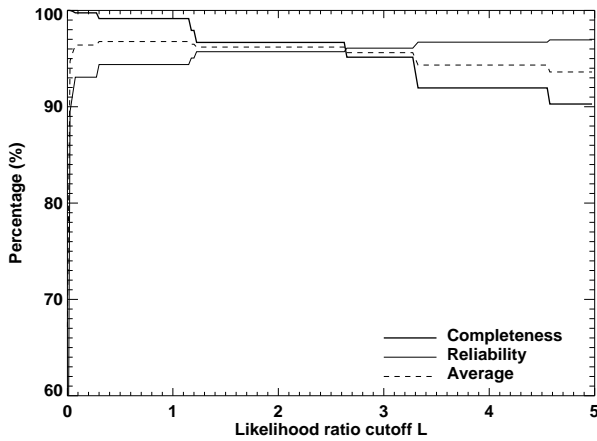
Figure B2. The completeness and reliability of the optical identifications as a function of the likelihood ratio cut-off, for all of the radio sources with a well defined position for their nucleus.

Bright radio source samples such as the revised 3CR sample (Laing et al. 1983), for which optical identifications have been made for essentially all sources, are known to frequently have two radio lobes of unequal length, or to show a bend in their radio jets. These parameters can be quantified as the *separation quotient*, $Q = \theta_1/\theta_2$, where θ_1 and θ_2 are the angular distances from the cores to the hotspots of the longer and shorter lobes respectively, and the *asymmetry angle*, ξ, that is defined as $180°$ minus the observed angle between vectors drawn from the nucleus of the radio source to the hotspots. From these two parameters and the size of the radio source ($D_{\rm rad} = \theta_1 + \theta_2$, assuming that ξ is small), expressions can be derived for the expected displacement of the central optical object along and perpendicular to (respectively) the main radio axis that connects the two hotspots:

$$\sigma_Q = \frac{1}{2}(\theta_1 - \theta_2) = \frac{1}{2}D_{\rm rad}\left(\frac{Q-1}{Q+1}\right), \qquad \sigma_\xi \approx \frac{1}{2}D_{\rm rad}\tan\frac{\xi}{2}$$

assuming that Q is close to unity and ξ is relatively small.

Best et al. (1995) investigated the distribution of Q and ξ within a complete subsample of 95 radio sources from the revised 3CR sample. They find mean values of $\overline{Q} = 1.42$ and $\overline{\xi} = 6.8°$; these mean values were adopted as input for the determination of the revised positional uncertainties of the extended radio sources in the sample[§], according to:

$$\sigma_{\alpha_{\rm rad}}^2 = 1''^2 + (\sigma_Q\sin{\rm PA})^2 + (\sigma_\xi\cos{\rm PA})^2$$

$$\sigma_{\delta_{\rm rad}}^2 = 1''^2 + (\sigma_Q\cos{\rm PA})^2 + (\sigma_\xi\sin{\rm PA})^2$$

where PA is the position angle of the radio source and the 1.0 arcsecond term corresponds to the uncertainties in the measurement of the radio source positions; this was the only term used in the analysis of the single component sources, where a value of 0.3 arcsec was adopted. A larger value is adopted here to account for the increased uncertainty in measuring the precise positions of the lobes, since these structures are extended and faint, but in most cases this term is negligible anyway.

Adopting these values for the radio positional uncertainties of each source, the likelihood analysis was repeated for the extended radio sources considering all optical counterparts within $0.25D_{\rm rad}$

[§] One important point to note with this analysis, however, is that although Best et al. (1995) find no evidence for any dependence of Q or ξ upon radio luminosity, the current sample is of significantly lower luminosity, and is selected at 1.4 GHz instead of at 178 MHz. Therefore the distributions of Q and ξ may not be entirely appropriate, which could potentially bias the statistics of this investigation.
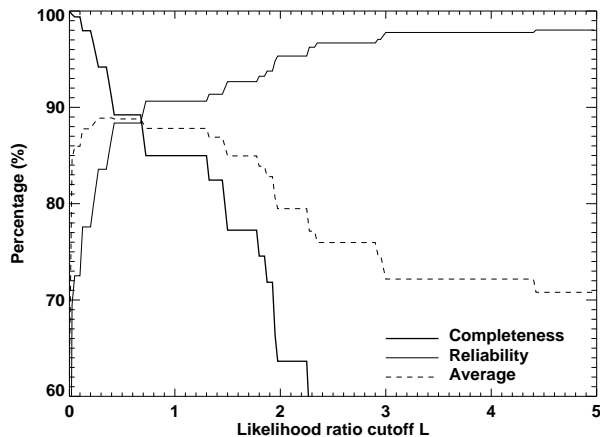
Figure B3. The completeness and reliability of the optical identifications as a function of the likelihood ratio cut-off, for the extended radio sources with no well–defined nucleus.

or $10''$ (whichever was larger) of the position midway between the two radio hotspots. A value of $\phi = 0.63$ was adopted, as for the single–component sources; this ignores the possibility that the redshift or magnitude distribution of the extended sources may be different from that of the unresolved sources, but there is no better approximation that can be made, and the overall results vary only slightly if the value of ϕ is changed.

The resulting dependence of the completeness and reliability of the identified optical hosts are shown in Figure B3 as a function of the likelihood ratio cut–off. The situation is understandably worse than in the previous case, due to the larger uncertainties in the radio position. At the peak in the average of the two functions, $L \approx 0.3$, the completeness of the optical identifications is $\sim 94\%$ and the reliability $\sim 84\%$. Optical counterparts above this threshold were found for 34 sources, with two potential counterparts above the threshold in 2 cases.

It was further noted that for 6 of the sources (see Table B1) for which no optical counterpart with a likelihood ratio above the cut–off were found, clear optical counterparts were seen to be associated with one of the two apparent radio lobes. These optical galaxies are also accepted as possible identifications, due to the possibility of radio sources with very asymmetric flux ratios, where the detected "lobe" is actually the radio core and a fainter lobe on the other side is not detected in the new radio observations.

APPENDIX C: THE FINAL CENSORS SAMPLE

Table C1 provides the definition of the final CENSORS sample.

Table B1. EIS optical counterparts of the radio sources. These were identified by maximum likelihood analysis on unresolved radio sources or those with unambiguous radio cores (class 1, likelihood $L > 1$ for for inclusion), maximum likelihood analysis on extended sources (class 2, $L > 0.3$ for inclusion), or inclusion because the optical counterpart lay directly on top of one of the radio components which could plausibly be a radio core (class 3). The optical magnitudes and uncertainties are taken from the EIS catalogues (see text for details), and the stellaricity classification (S/G; see text for details) is taken from the EIS I–band observations. Notes are attached in the text for sources marked with an 'N'

Source	Class	L	RA (J2000) Dec	I-magnitude	V-magnitude	B-magnitude	S/G	Notes
EISD1	2	11.35	09 51 29.22 -20 50 30.7	21.74 ± 0.10	22.93 ± 0.09	23.27 ± 0.09	0.26	
EISD2	1	77.73	09 46 50.22 -20 20 44.4	22.59 ± 0.18		24.02 ± 0.17	0.01	
EISD3	1	5.81	09 50 31.40 -21 02 44.4	20.60 ± 0.20	23.11 ± 0.11	23.77 ± 0.16	0.02	N
EISD6	2	2.91	09 49 53.26 -21 56 19.9	21.30 ± 0.08	23.36 ± 0.12	23.41 ± 0.13	0.00	N
	2	2.39	09 49 53.23 -21 56 22.0	22.58 ± 0.15			0.29	
EISD7	1	38.80	09 51 43.60 -21 23 57.9	18.26 ± 0.01	18.65 ± 0.01	18.40 ± 0.01	1.00	
EISD8	1	1.22	09 53 44.47 -21 36 01.7	22.15 ± 0.12	22.73 ± 0.06	22.57 ± 0.15	0.19	
EISD10	1	3.31	09 45 56.68 -21 16 53.6	22.62 ± 0.17	23.54 ± 0.19	23.38 ± 0.11	0.64	
EISD11	1	2.65	09 57 30.06 -21 30 58.9	17.77 ± 0.01	19.38 ± 0.02	20.35 ± 0.03	0.25	
EISD12	1	37.18	09 49 35.46 -21 56 23.3	18.28 ± 0.01	20.08 ± 0.01	20.96 ± 0.02	0.03	
EISD15	1	19.77	09 53 29.55 -20 02 12.6	21.75 ± 0.07	22.49 ± 0.05	22.74 ± 0.05	0.91	
EISD16	2	0.31	09 47 27.00 -21 26 33.4	18.26 ± 0.01	18.73 ± 0.01	19.15 ± 0.01	0.99	N
EISD18	1	24.93	09 46 41.13 -20 29 26.7	21.88 ± 0.09	23.35 ± 0.15	23.90 ± 0.19	0.00	
EISD21	2	6.34	09 54 47.59 -20 59 44.3	23.60 ± 0.25			0.58	
EISD22	2	5.50	09 46 50.99 -20 53 18.2	20.57 ± 0.06	20.91 ± 0.04	21.45 ± 0.03	0.00	
EISD24	2	8.45	09 52 43.02 -19 58 21.6	21.38 ± 0.07	23.63 ± 0.14		0.15	
EISD25	1	12.94	09 55 13.59 -21 23 02.4	14.88 ± 0.00	16.13 ± 0.01	16.96 ± 0.01	0.03	
EISD28	1	41.89	09 47 58.95 -21 21 50.5	22.11 ± 0.10	24.38 ± 0.19	24.52 ± 0.14	0.26	
EISD38	3	N/A	09 46 32.15 -20 26 15.5	19.02 ± 0.02	20.86 ± 0.04	21.59 ± 0.03	0.03	N
EISD39	1	32.38	09 48 15.74 -21 40 06.1	18.73 ± 0.01	19.02 ± 0.01	19.23 ± 0.01	0.97	
EISD40	1	7.02	09 45 55.92 -20 28 29.7	16.41 ± 0.00	18.58 ± 0.01	19.50 ± 0.05	0.86	
EISD43	2	1.45	09 51 40.85 -20 11 16.3	22.25 ± 0.12			0.00	
EISD44	1	6.79	09 51 49.83 -21 24 57.5	18.29 ± 0.01	20.12 ± 0.02	21.14 ± 0.02	0.03	
EISD47	1	5.78	09 47 53.61 -21 47 19.3	24.95 ± 0.63			0.36	N
EISD48	2	12.52	09 54 52.46 -21 19 28.6	18.71 ± 0.01	21.11 ± 0.03	22.12 ± 0.04	0.03	
EISD51	1	16.75	09 49 33.24 -21 27 07.7	22.90 ± 0.17		24.74 ± 0.16	0.68	
EISD52	2	1.87	09 49 19.57 -21 51 34.1	23.67 ± 0.19	24.55 ± 0.26	24.52 ± 0.20	0.44	
EISD54	2	1.78	09 48 36.08 -21 06 22.4	20.60 ± 0.03	21.73 ± 0.03	21.61 ± 0.02	0.92	
EISD55	2	2.35	09 50 59.01 -21 14 24.4	21.54 ± 0.10	23.18 ± 0.13	23.66 ± 0.12	0.00	
EISD58	1	15.30	09 49 18.16 -20 54 44.8	17.10 ± 0.01	18.92 ± 0.03	20.09 ± 0.01	0.03	
EISD60	3	N/A	09 52 01.59 -21 15 53.0	23.70 ± 0.19		25.06 ± 0.28	0.49	N
EISD62	1	47.94	09 54 27.09 -20 29 46.6	19.85 ± 0.02	20.48 ± 0.01	20.80 ± 0.02	0.98	
EISD63	2	0.70	09 47 03.25 -20 50 00.8	19.34 ± 0.02	21.08 ± 0.02	21.82 ± 0.04	0.02	
EISD64	2	11.64	09 52 59.15 -21 48 42.5	20.93 ± 0.05	24.37 ± 0.14		0.24	
EISD65	1	32.03	09 54 03.05 -20 25 13.1	20.39 ± 0.05	22.70 ± 0.10	23.53 ± 0.13	0.01	
EISD66	1	8.08	09 57 42.91 -20 06 36.9	20.50 ± 0.04	23.33 ± 0.10	24.16 ± 0.15	0.04	
EISD67	1	40.69	09 53 23.21 -20 13 43.5	19.20 ± 0.02	20.57 ± 0.16	20.55 ± 0.01	0.04	
EISD68	1	14.13	09 54 28.32 -20 39 26.9	19.48 ± 0.02	20.44 ± 0.01	20.41 ± 0.01	0.97	
EISD71	2	2.25	09 49 30.81 -20 23 34.7	19.61 ± 0.03	22.00 ± 0.18	22.94 ± 0.11	0.03	
EISD74	1	21.23	09 53 20.60 -21 43 58.9	15.75 ± 0.00	17.43 ± 0.01	18.59 ± 0.01	0.03	
EISD76	2	10.61	09 51 32.39 -21 00 29.0	17.50 ± 0.01	19.89 ± 0.02	20.95 ± 0.05	0.03	
EISD78	2	0.35	09 50 43.16 -21 26 41.3	22.58 ± 0.14			0.04	
EISD80	2	7.00	09 51 21.03 -21 29 54.8	22.19 ± 0.13			0.14	
EISD81	1	1.17	09 48 42.52 -21 52 24.8	21.69 ± 0.10			0.00	
EISD83	1	29.40	09 51 48.67 -20 31 52.4	23.48 ± 0.26			0.20	
EISD84	2	09.66	09 49 45.86 -21 50 06.5	20.25 ± 0.03	22.94 ± 0.07	24.30 ± 0.14	0.04	
EISD88	2	7.58	09 45 29.53 -21 18 51.7	17.96 ± 0.01	19.96 ± 0.01	20.89 ± 0.01	0.98	
EISD89	2	1.95	09 57 31.77 -21 20 29.2	18.62 ± 0.01	20.87 ± 0.03	21.95 ± 0.04	0.03	
EISD90	1	2.55	09 50 46.42 -21 32 55.7	21.96 ± 0.11	22.47 ± 0.06	23.34 ± 0.13	0.25	
EISD91	3	N/A	09 54 51.95 -21 30 16.4	19.88 ± 0.20	21.54 ± 0.20	22.55 ± 0.20	0.02	N
EISD98	2	1.49	09 45 26.93 -20 33 52.8	16.73 ± 0.01	18.37 ± 0.01	19.88 ± 0.01	0.03	
EISD102	3	N/A	09 57 46.06 -21 23 27.7	17.23 ± 0.01	18.99 ± 0.01	20.16 ± 0.01	0.03	N
EISD104	1	66.46	09 49 42.99 -20 37 45.6	23.60 ± 0.20		24.99 ± 0.31	0.53	
EISD105	2	2.98	09 54 16.45 -21 29 04.3	21.16 ± 0.06	22.44 ± 0.08	22.87 ± 0.08	0.13	
EISD106	1	48.67	09 45 48.50 -21 59 06.1	22.57 ± 0.15		24.27 ± 0.19	0.16	
EISD107	2	10.73	09 55 59.27 -20 42 52.8	19.24 ± 0.02	21.05 ± 0.03	22.27 ± 0.05	0.03	
EISD110	3	N/A	09 54 53.46 -21 15 13.1	20.01 ± 0.02	21.25 ± 0.03	23.94 ± 0.05	0.03	N
EISD113	2	4.42	09 50 53.09 -21 33 04.0	14.49 ± 0.00	14.39 ± 0.01	14.65 ± 0.01	0.98	
EISD116	1	72.10	09 51 29.71 -20 16 42.8	20.13 ± 0.03	21.72 ± 0.08	22.77 ± 0.10	0.02	
EISD120	1	N/A	09 48 04.32 -20 34 36.3	23.00 ± 0.30			0.00	N

Table B1. *continued.* EIS optical counterparts of the radio sources.

Source	Class	L	RA (J2000) Dec	I-magnitude	V-magnitude	B-magnitude	S/G	Notes
EISD122	1	43.12	09 52 55.92 -20 51 45.0	18.68 ± 0.01	19.29 ± 0.01	19.41 ± 0.01	0.97	
EISD123	3	N/A	No position obtainable	Saturated	Saturated	Saturated	0.00	N
EISD126	2	1.94	09 54 36.24 -21 44 30.9	22.54 ± 0.14			0.07	
EISD127	1	17.18	09 48 22.19 -21 05 08.4	22.43 ± 0.12			0.00	
EISD132	2	5.74	09 46 19.15 -20 37 57.7	17.41 ± 0.01	18.86 ± 0.01	19.84 ± 0.01	0.03	
EISD133	1	7.56	09 57 02.29 -21 56 51.2	19.49 ± 0.03	22.22 ± 0.07	24.15 ± 0.14	0.03	
EISD134	2	0.68	09 46 49.47 -21 16 46.4	18.36 ± 0.01	20.83 ± 0.02	21.82 ± 0.04	0.03	
EISD136	1	22.21	09 50 48.54 -21 54 56.7	23.77 ± 0.25	24.69 ± 0.18	24.60 ± 0.22	0.65	
EISD137	1	11.63	09 48 14.19 -19 59 56.3	18.93 ± 0.02	20.84 ± 0.02	21.92 ± 0.04	0.03	
EISD139	1	15.07	09 52 50.42 -21 31 47.6	22.35 ± 0.14	24.33 ± 0.25		0.41	
EISD141	1	10.38	09 55 11.46 -20 30 19.2	17.52 ± 0.01	19.17 ± 0.01	20.25 ± 0.10	0.03	
EISD142	1	3.29	09 56 07.00 -20 05 44.3	21.96 ± 0.10	24.37 ± 0.18		0.02	
EISD143	1	78.31	09 57 35.36 -20 29 35.4	19.97 ± 0.02	20.57 ± 0.03	20.90 ± 0.02	0.97	
EISD145	2	2.25	09 57 39.07 -20 03 20.2	23.33 ± 0.19			0.74	
EISD146	1	51.27	09 56 42.30 -21 19 44.3	23.50 ± 0.23	23.90 ± 0.17	22.95 ± 0.07	0.51	
EISD148	3	N/A	09 45 38.08 -21 11 13.5	18.92 ± 0.02	21.38 ± 0.03	22.23 ± 0.05	0.03	N
EISD149	1	71.30	09 47 44.76 -21 12 23.4	18.34 ± 0.01	20.77 ± 0.02	21.73 ± 0.03	0.03	
EISD150	2	5.38	09 47 10.31 -20 35 52.4	22.10 ± 0.11	24.30 ± 0.24		0.07	
EISD153	1	48.44	09 56 49.79 -20 35 25.9	17.09 ± 0.01	18.63 ± 0.01	19.70 ± 0.01	0.03	
EISD155	3	N/A	09 57 24.90 -20 22 43.0	17.84 ± 0.01	20.10 ± 0.02	21.09 ± 0.02	0.03	N
EISD156	1	49.46	09 56 37.10 -20 19 05.8	16.94 ± 0.01	18.38 ± 0.01	19.60 ± 0.01	0.03	
EISD157	1	9.38	09 49 02.26 -21 15 05.1	23.58 ± 0.26		25.42 ± 0.19	0.48	
EISD159	1	9.01	09 53 57.43 -20 36 51.0	21.10 ± 0.06	22.28 ± 0.06	22.41 ± 0.05	0.31	
EISD162	3	N/A	09 56 39.22 -20 10 44.3	19.20 ± 0.30			—	N
EISD163	3	N/A	No position obtainable	Saturated	Saturated	Saturated	0.00	N
EISD164	1	42.18	09 52 01.22 -20 24 56.2	17.15 ± 0.01	18.58 ± 0.01	19.57 ± 0.01	0.03	
EISD165	2	11.66	09 54 10.51 -21 58 01.5	22.73 ± 0.15			0.11	
EISD166	1	82.75	09 56 04.45 -21 44 36.6	22.73 ± 0.22	23.62 ± 0.16	23.68 ± 0.10	0.48	
EISD169	2	1.31	09 51 49.02 -21 33 40.0	17.15 ± 0.01	19.50 ± 0.01	19.97 ± 0.02	0.03	
EISD171	2	1.94	09 47 50.33 -21 42 10.1	14.84 ± 0.00	14.99 ± 0.01	15.34 ± 0.01	0.98	N
	2	0.41	09 47 50.64 -21 42 11.4	17.43 ± 0.00	18.84 ± 0.01	19.34 ± 0.01	0.92	
EISD173	1	54.15	09 54 31.06 -20 35 37.7	21.05 ± 0.07	22.96 ± 0.14		0.00	
EISD174	1	28.36	09 49 02.79 -20 16 11.0	22.50 ± 0.13	22.97 ± 0.12	23.99 ± 0.12	0.26	
EISD175	2	2.96	09 49 22.34 -21 18 17.7	18.95 ± 0.02	21.83 ± 0.05	23.00 ± 0.25	0.03	
EISD177	1	80.27	09 55 26.95 -20 46 05.9	19.99 ± 0.04	22.63 ± 0.06	23.45 ± 0.13	0.05	
EISD178	3	N/A	09 47 47.93 -21 00 45.4	21.42 ± 0.08	22.63 ± 0.10	23.12 ± 0.06	0.52	N
EISD179	1	10.44	09 49 59.71 -21 27 18.3	19.95 ± 0.03	22.29 ± 0.07	22.60 ± 0.15	0.04	
EISD180	1	48.63	09 49 12.74 -22 00 23.4	17.61 ± 0.01	19.85 ± 0.02	20.81 ± 0.02	0.03	
EISD181	1	20.07	09 54 41.88 -20 49 43.4	24.85 ± 0.35			0.37	N
EISD185	1	14.39	09 52 14.36 -21 40 18.4	14.84 ± 0.00	15.87 ± 0.01	16.15 ± 0.01	0.04	
EISD186	1	35.36	09 49 24.62 -21 11 11.6	20.77 ± 0.04	22.83 ± 0.07	23.10 ± 0.10	0.04	
EISD187	2	0.42	09 50 38.66 -21 41 11.4	18.73 ± 0.02	21.49 ± 0.05	22.43 ± 0.08	0.03	
EISD191	3	N/A	No position obtainable	Saturated	Saturated	Saturated	0.00	N
EISD199	1	53.54	09 45 26.32 -21 55 00.1	17.99 ± 0.01	19.64 ± 0.01	20.71 ± 0.02	0.03	

Table C1. Definition of the final CENSORS sample. This includes only those NVSS sources which are real and fall within the EIS Patch D. It is numbered in order of decreasing flux density, as determined from the latest NVSS catalogue (version 2.17), although those sources marked with an asterisk have had their NVSS flux densities adjusted to account for overlap with another NVSS source. Four additional sample members are appended, as discussed in the text.

New name	Old name	$S^{\mathrm{NVSS}}_{1.4\,\mathrm{GHz}}$ (mJy)	New name	Old name	$S^{\mathrm{NVSS}}_{1.4\,\mathrm{GHz}}$ (mJy)	New name	Old name	$S^{\mathrm{NVSS}}_{1.4\,\mathrm{GHz}}$ (mJy)
CENSORS1	EISD1	659.5 ± 19.8	CENSORS53	EISD76	21.6 ± 1.1	CENSORS105	EISD138	10.6 ± 0.6
CENSORS2	EISD2	452.3 ± 13.6	CENSORS54	EISD74	21.4 ± 0.8	CENSORS106	EISD142	10.5 ± 0.6
CENSORS3	EISD3	355.3 ± 10.7	CENSORS55	EISD71	21.4 ± 0.8	CENSORS107	EISD148	10.3 ± 1.0
CENSORS4	EISD6	283.0 ± 9.5	CENSORS56	EISD78	20.8 ± 1.1	CENSORS108	EISD153	10.2 ± 0.6
CENSORS5	EISD8	244.7 ± 8.2	CENSORS57	EISD80	20.7 ± 1.1	CENSORS109	EISD154	10.1 ± 0.6
CENSORS6	EISD7*	239.7 ± 1.3	CENSORS58	EISD79	20.7 ± 0.8	CENSORS110	EISD141	10.1 ± 1.3
CENSORS7	EISD10	148.2 ± 5.1	CENSORS59	EISD81	19.1 ± 1.1	CENSORS111	EISD149	10.0 ± 0.6
CENSORS8	EISD11	126.3 ± 3.8	CENSORS60	EISD83	18.9 ± 0.7	CENSORS112	EISD146	9.8 ± 0.6
CENSORS9	EISD12	118.2 ± 3.6	CENSORS61	EISD82	18.5 ± 0.7	CENSORS113	EISD150	9.7 ± 0.6
CENSORS10	EISD16	79.4 ± 2.9	CENSORS62	EISD84	18.4 ± 0.7	CENSORS114	EISD166	9.6 ± 0.6
CENSORS11	EISD15	78.1 ± 2.4	CENSORS63	EISD88	18.3 ± 0.7	CENSORS115	EISD155	9.6 ± 1.0
CENSORS12	EISD18	70.4 ± 2.6	CENSORS64	EISD85	18.1 ± 1.0	CENSORS116	EISD143	9.6 ± 0.6
CENSORS13	EISD20	66.3 ± 2.7	CENSORS65	EISD87	17.9 ± 1.0	CENSORS117	EISD165	9.5 ± 0.6
CENSORS14	EISD21	65.6 ± 2.4	CENSORS66	EISD90	17.4 ± 1.1	CENSORS118	EISD161	9.4 ± 0.6
CENSORS15	EISD22	63.0 ± 1.9	CENSORS67	EISD89	17.3 ± 0.7	CENSORS119	EISD157	9.4 ± 0.6
CENSORS16	EISD23	61.7 ± 2.3	CENSORS68	EISD91	17.2 ± 0.7	CENSORS120	EISD159	9.1 ± 0.6
CENSORS17	EISD24	61.5 ± 2.3	CENSORS69	EISD92	17.0 ± 0.7	CENSORS121	EISD164	9.0 ± 0.5
CENSORS18	EISD25	58.3 ± 1.8	CENSORS70	EISD124*	17.0 ± 2.0	CENSORS122	EISD156	9.0 ± 0.6
CENSORS19	EISD27	55.1 ± 2.1	CENSORS71	EISD93	16.7 ± 0.7	CENSORS123	EISD173	8.7 ± 0.5
CENSORS20	EISD30	54.2 ± 2.1	CENSORS72	EISD97	16.5 ± 0.7	CENSORS124	EISD163	8.7 ± 0.6
CENSORS21	EISD28	54.0 ± 1.7	CENSORS73	EISD94	16.2 ± 0.7	CENSORS125	EISD175	8.4 ± 0.5
CENSORS22	EISD29	52.9 ± 1.7	CENSORS74	EISD96	16.0 ± 0.7	CENSORS126	EISD171	8.4 ± 1.3
CENSORS23	EISD31	52.4 ± 2.0	CENSORS75	EISD98	15.7 ± 1.0	CENSORS127	EISD186	8.3 ± 0.5
CENSORS24	EISD32	51.0 ± 1.6	CENSORS76	EISD102	15.3 ± 0.7	CENSORS128	EISD174	8.3 ± 0.5
CENSORS25	EISD34	49.2 ± 1.9	CENSORS77	EISD104	15.0 ± 0.7	CENSORS129	EISD170	8.3 ± 0.6
CENSORS26	EISD36	44.4 ± 1.4	CENSORS78	EISD107	14.6 ± 0.7	CENSORS130	EISD172	8.2 ± 0.5
CENSORS27	EISD44*	40.4 ± 2.3	CENSORS79	EISD106	14.6 ± 1.1	CENSORS131	EISD169	8.2 ± 0.6
CENSORS28	EISD38	40.1 ± 1.9	CENSORS80	EISD110	14.5 ± 0.6	CENSORS132	EISD167	7.9 ± 0.6
CENSORS29	EISD39	38.2 ± 1.6	CENSORS81	EISD105	14.5 ± 1.4	CENSORS133	EISD183	7.8 ± 1.2
CENSORS30	EISD40	37.8 ± 2.0	CENSORS82	EISD113	13.6 ± 0.6	CENSORS134	EISD182	7.8 ± 0.6
CENSORS31	EISD41	37.3 ± 1.5	CENSORS83	EISD116	13.5 ± 0.6	CENSORS135	EISD178	7.8 ± 0.6
CENSORS32	EISD43	35.3 ± 1.5	CENSORS84	EISD103	13.5 ± 1.2	CENSORS136	EISD181	7.5 ± 0.6
CENSORS33	EISD45	34.3 ± 1.1	CENSORS85	EISD112	13.4 ± 1.0	CENSORS137	EISD187	7.4 ± 1.2
CENSORS34	EISD47	34.2 ± 1.1	CENSORS86	EISD120	13.2 ± 0.6	CENSORS138	EISD177	7.1 ± 0.6
CENSORS35	EISD48	34.1 ± 1.4	CENSORS87	EISD111	13.2 ± 0.6	CENSORS139	EISD180	6.9 ± 0.6
CENSORS36	EISD51	32.3 ± 1.1	CENSORS88	EISD119	13.1 ± 0.6	CENSORS140	EISD199	6.8 ± 0.5
CENSORS37	EISD52	31.8 ± 1.4	CENSORS89	EISD117	13.0 ± 1.0	CENSORS141	EISD189	6.6 ± 0.6
CENSORS38	EISD53	31.7 ± 1.1	CENSORS90	EISD114	12.8 ± 0.6	CENSORS142	EISD195	6.3 ± 0.6
CENSORS39	EISD54	31.5 ± 1.1	CENSORS91	EISD127	12.7 ± 0.6	CENSORS143	EISD188	6.1 ± 0.6
CENSORS40	EISD55	30.9 ± 1.3	CENSORS92	EISD122	12.6 ± 1.1	CENSORS144	EISD179	6.0 ± 0.6
CENSORS41	EISD58	27.5 ± 1.7	CENSORS93	EISD132	12.2 ± 0.6	CENSORS145	EISD137*	5.8 ± 0.3
CENSORS42	EISD60	26.5 ± 0.9	CENSORS94	EISD125	12.2 ± 0.6	CENSORS146	EISD191	5.4 ± 0.6
CENSORS43	EISD64	26.4 ± 0.9	CENSORS95	EISD123	12.2 ± 1.2	CENSORS147	EISD197	4.2 ± 0.7
CENSORS44	EISD62	26.1 ± 0.9	CENSORS96	EISD131	12.0 ± 0.6	CENSORS148	EISD162	4.1 ± 0.8
CENSORS45	EISD66	25.5 ± 1.2	CENSORS97	EISD126	12.0 ± 1.2	CENSORS149	EISD185	4.0 ± 0.7
CENSORS46	EISD65	25.2 ± 0.9	CENSORS98	EISD130	11.8 ± 0.6	CENSORS150	EISD194	3.8 ± 0.7
CENSORS47	EISD63	25.2 ± 0.9	CENSORS99	EISD133	11.6 ± 0.6	CENSORS-X1	J094651-2125	7.2 ± 0.5
CENSORS48	EISD68	24.2 ± 0.9	CENSORS100	EISD136	11.5 ± 0.6	CENSORS-X2	J095233-2129	6.8 ± 0.5
CENSORS49	EISD67	23.8 ± 0.9	CENSORS101	EISD139	11.4 ± 0.6	CENSORS-X3	J095240-2123	6.7 ± 0.5
CENSORS50	EISD69	22.3 ± 0.8	CENSORS102	EISD134	11.1 ± 1.1	CENSORS-D1	J095218-2038	3.6 ± 0.6
CENSORS51	EISD75	21.7 ± 0.8	CENSORS103	EISD56*	10.7 ± 0.6		J095223-2041	3.8 ± 0.7
CENSORS52	EISD72	21.7 ± 0.8	CENSORS104	EISD145	10.7 ± 0.6			

This figure "FigA1_1.jpg" is available in "jpg" format from:

http://arXiv.org/ps/astro-ph/0308401v1

This figure "FigA2_1.jpg" is available in "jpg" format from:

http://arXiv.org/ps/astro-ph/0308401v1

This figure "FigA1_2.jpg" is available in "jpg" format from:

http://arXiv.org/ps/astro-ph/0308401v1

This figure "FigA2_2.jpg" is available in "jpg" format from:

http://arXiv.org/ps/astro-ph/0308401v1

This figure "Fig3.jpg" is available in "jpg" format from:

http://arXiv.org/ps/astro-ph/0308401v1

This figure "FigA1_3.jpg" is available in "jpg" format from:

http://arXiv.org/ps/astro-ph/0308401v1

This figure "FigA2_3.jpg" is available in "jpg" format from:

http://arXiv.org/ps/astro-ph/0308401v1

This figure "FigA3.jpg" is available in "jpg" format from:

http://arXiv.org/ps/astro-ph/0308401v1

This figure "Fig4.jpg" is available in "jpg" format from:

http://arXiv.org/ps/astro-ph/0308401v1

This figure "FigA1_4.jpg" is available in "jpg" format from:

http://arXiv.org/ps/astro-ph/0308401v1

This figure "Fig5.jpg" is available in "jpg" format from:

http://arXiv.org/ps/astro-ph/0308401v1

This figure "FigA1_5.jpg" is available in "jpg" format from:

http://arXiv.org/ps/astro-ph/0308401v1

This figure "Fig6.jpg" is available in "jpg" format from:

http://arXiv.org/ps/astro-ph/0308401v1

This figure "FigA1_6.jpg" is available in "jpg" format from:

http://arXiv.org/ps/astro-ph/0308401v1

This figure "Fig7.jpg" is available in "jpg" format from:

http://arXiv.org/ps/astro-ph/0308401v1

This figure "FigA1_7.jpg" is available in "jpg" format from:

http://arXiv.org/ps/astro-ph/0308401v1

This figure "Fig8.jpg" is available in "jpg" format from:

http://arXiv.org/ps/astro-ph/0308401v1

This figure "FigA1_8.jpg" is available in "jpg" format from:

http://arXiv.org/ps/astro-ph/0308401v1

This figure "Fig9.jpg" is available in "jpg" format from:

http://arXiv.org/ps/astro-ph/0308401v1

This figure "FigA1_9.jpg" is available in "jpg" format from:

http://arXiv.org/ps/astro-ph/0308401v1

This figure "FigA1_10.jpg" is available in "jpg" format from:

http://arXiv.org/ps/astro-ph/0308401v1

This figure "FigA1_11.jpg" is available in "jpg" format from:

http://arXiv.org/ps/astro-ph/0308401v1

This figure "FigA1_12.jpg" is available in "jpg" format from:

http://arXiv.org/ps/astro-ph/0308401v1

This figure "FigA1_13.jpg" is available in "jpg" format from:

http://arXiv.org/ps/astro-ph/0308401v1

This figure "FigA1_14.jpg" is available in "jpg" format from:

http://arXiv.org/ps/astro-ph/0308401v1

This figure "FigA1_15.jpg" is available in "jpg" format from:

http://arXiv.org/ps/astro-ph/0308401v1

This figure "FigA1_16.jpg" is available in "jpg" format from:

http://arXiv.org/ps/astro-ph/0308401v1

This figure "FigA1_17.jpg" is available in "jpg" format from:

http://arXiv.org/ps/astro-ph/0308401v1

This figure "FigA1_18.jpg" is available in "jpg" format from:

http://arXiv.org/ps/astro-ph/0308401v1

This figure "FigA1_19.jpg" is available in "jpg" format from:

http://arXiv.org/ps/astro-ph/0308401v1

This figure "FigA1_20.jpg" is available in "jpg" format from:

http://arXiv.org/ps/astro-ph/0308401v1

This figure "FigA1_21.jpg" is available in "jpg" format from:

http://arXiv.org/ps/astro-ph/0308401v1

This figure "FigA1_22.jpg" is available in "jpg" format from:

http://arXiv.org/ps/astro-ph/0308401v1

This figure "FigA1_23.jpg" is available in "jpg" format from:

http://arXiv.org/ps/astro-ph/0308401v1

This figure "FigA1_24.jpg" is available in "jpg" format from:

http://arXiv.org/ps/astro-ph/0308401v1

This figure "FigA1_25.jpg" is available in "jpg" format from:

http://arXiv.org/ps/astro-ph/0308401v1